JGR Solid Earth

RESEARCH ARTICLE
10.1029/2025JB032816

Magnetic Signature of Active Hydrothermal Systems in a Volcanic-Evaporitic Environment in the Danakil Depression

Hanjin Choe[1], **Jerome Dyment**[2], **and Daniel Mège**[3,4]

[1]Department of Geological Sciences and Institute of Geohazard Research, Pusan National University, Busan, Republic of Korea, [2]Université Paris Cité, Institut de physique du globe de Paris, CNRS, Paris, France, [3]Centrum Badań Kosmicznych Polskiej Akademii Nauk (CBK PAN), Warszawa, Poland, [4]Physikalisches Institut, Universität Bern, Bern, Switzerland

Abstract Hydrothermal systems in volcanic-evaporitic environments provide unique insights into subsurface geological processes, yet their magnetic signature remains poorly understood. Here we suggest that hydrothermal activity in the Dallol area of Ethiopia produces distinct magnetic patterns that may reflect both physical and chemical modifications of the subsurface. Through high-resolution near-surface magnetic surveys, we identify weak positive anomalies associated with reddish brine mud layer and negative amplitude anomalies (~20 nT) over active hydrothermal features. These patterns suggest that hydrothermalism consistently results in weakening magnetization through mechanical destruction and chemical alteration of substrates, providing insights into fluid circulation and their relationship with tectonic processes. Our findings support that near-surface magnetic surveys can effectively map active hydrothermal systems across diverse geological settings from volcanic-evaporitic environments to mid-ocean ridges with important implications for understanding geothermal exploration, and the evolution of divergent plate boundaries.

Plain Language Summary The Dallol area in Ethiopia, located at a divergent plate boundary, presents a unique geological setting with active volcanism, tectonics, and hydrothermal activity. Our study used high-resolution near-surface magnetic surveys to investigate how these processes influence underground magnetization. We identified that reddish salty mud layer, likely formed from iron-rich volcanic ashes, produce weak positive magnetic anomalies. In contrast, active hydrothermal features, such as bubbling pools and fissures, exhibit negative magnetic signals (around 20 nT). This implies that hydrothermal activity weakens the magnetization by breaking down minerals and altering their chemical composition. Our results support that magnetic surveys are a valuable tool for detecting and mapping active hydrothermal systems. These findings have important implications for geothermal exploration and understanding how geological features evolve in volcanic-salt environments and other tectonically active regions, such as mid-ocean ridges.

Key Points:

- The short-wavelengths of a near-surface magnetic survey in the Dallol area, Ethiopia, provides information on shallow geological processes
- Reddish brine mud layer outcropping in the Island Dome, a <1 m elevation, are slightly magnetized and generate positive magnetic anomalies
- Hydrothermal manifestations result in physical and/or chemical alteration of the reddish brine mud layer and appear as magnetic anomaly lows

Supporting Information:

Supporting Information may be found in the online version of this article.

Correspondence to:

H. Choe,
explorist@pusan.ac.kr

Citation:

Choe, H., Dyment, J., & Mège, D. (2025). Magnetic signature of active hydrothermal systems in a volcanic-evaporitic environment in the Danakil Depression. *Journal of Geophysical Research: Solid Earth*, *130*, e2025JB032816. https://doi.org/10.1029/2025JB032816

Received 22 AUG 2025
Accepted 1 DEC 2025

Author Contributions:

Conceptualization: Jerome Dyment, Daniel Mège
Data curation: Hanjin Choe
Formal analysis: Hanjin Choe, Jerome Dyment, Daniel Mège
Investigation: Hanjin Choe, Daniel Mège
Methodology: Hanjin Choe
Resources: Hanjin Choe, Daniel Mège
Validation: Hanjin Choe
Visualization: Hanjin Choe
Writing – original draft: Hanjin Choe
Writing – review & editing: Jerome Dyment

1. Introduction

Hydrothermal circulation is observed wherever a heat source, generally volcanism, and fractures in the crust meet water. It is a widespread phenomenon on Earth and plays a fundamental role in various geological processes such as mineral alteration (Choe & Dyment, 2020, 2021; Heap et al., 2021), ore concentration (M. K. Tivey, 2007), rock deformation (Cox, 2005; Sibson, 1996), and the weakening of seismogenic zones (Pereira et al., 2024). These processes are particularly significant in tectonically active regions, where hydrothermal systems can drive large-scale geophysical and environmental changes. Divergent plate boundaries, whether at mid-ocean ridges or incipient rift zones, provide unique opportunities to study these dynamic processes. Understanding how these systems evolve over time can shed light on the Earth's tectonic evolution (Alt, 1995; Lister, 1972; Illsley-kemp et al., 2018), geothermal energy potential (Franzson et al., 2015; Scott et al., 2019), and the environmental impacts (Lutz & Kennish, 1993; Ogubazghi et al., 2004; Zierenberg et al., 2000) of hydrothermal activity.

Magnetic surveys have proven a valuable geophysical tool in characterizing hydrothermal systems at various scales (Szitkar, Dyment, Fouquet, et al., 2014; M. A. Tivey & Dyment, 2010; M. A. Tivey et al., 1993). Previous studies at mid-ocean ridges have shown that hydrothermal activity can significantly modify the rock magnetic properties through thermal demagnetization, alteration of pre-existing magnetization, or formation of new magnetic minerals (Szitkar, Dyment, Choi, & Fouquet, 2014; Szitkar, Dyment, Fouquet, et al., 2014; M. A. Tivey & Dyment, 2010). However, the expression of these processes at high resolution in continental settings, particularly in volcanic-evaporitic environments, is not well understood. While such knowledge would enhance our understanding of fluid circulation patterns and their relationship with tectonic processes across different

geological contexts, suitable study areas are rare. The Yellow Lake Fissure (YLF) area offers an accessible site to study the magnetic signature of hydrothermal systems within a volcanic-evaporitic context. The Danakil Depression in northern Afar, where the divergent boundary between the Nubian and Danakil microplates intersects with active volcanism and complex tectonic dynamics (Bastow et al., 2018; Hurman et al., 2023; Le Gall et al., 2018; Mège et al., 2023), represents an ideal natural laboratory to address these questions. In this area, the Dallol dome presents a hydrothermal environment characterized by hyper-acidic fluids and hypersaline lakes (Cavalazzi et al., 2019; Kotopoulou et al., 2019; Otálora et al., 2022). These extreme environmental conditions make it a key site for studying how tectonic activity influences hydrothermal circulation (Franzson et al., 2015; Otálora et al., 2022), sedimentation (Carniel et al., 2010), and biological activity (Belilla et al., 2021). The YLF, located southeast of the dome, provides direct observation to hydrothermal systems and the associated structural discontinuities (La Rosa et al., 2023; Xu et al., 2020), facilitating investigation into the tectonic-hydrothermal relationships at multiple scales.

This study presents the results of a high-resolution magnetic anomaly survey conducted in the northern part of the YLF system, an area influenced by ongoing hydrothermal activity and evaporitic sedimentation. By analyzing magnetic anomalies in this unique setting, we aim to deepen our understanding of the processes controlling hydrothermal circulation and their broader geological implications. Additionally, the extreme environmental conditions and distinctive geological context of the Dallol area offer a valuable case study for exploring the wider environmental impacts of hydrothermal activity on Earth's surface processes.

2. Earlier Geological Works

The YLF, located southeast of the Dallol dome (Figure 1), lies parallel to a Black Mountain Dike that was injected eastward from Dallol in 2004 (Nobile et al., 2012). This dike injection, likely originating from a magma body beneath the Dallol dome (Albino & Biggs, 2021), coincided with hydrothermal activity at the YLF and was soon followed by a tectonic event along the fault (Mège et al., 2023). Brittle deformation revealed two dominant trends: the primary N-S trend of the YLF and a NW-SE trend (Figure 1c). This dike and fissure system is associated with recent activity along the divergent plate boundary between the Nubian plate to the west and the Danakil microplate to the east.

Analysis of a 1965 Corona-4A satellite image (2.4 m/pixel resolution) reveals that four key structural and morphological features of the YLF were already present (Mège et al., 2023):

1. Consistent YLF Trend: The primary north-south structural trend of the YLF is clearly visible in the 1965 imagery and remains consistent in subsequent images, indicating no significant reactivation between 1965 and 2004–2005.
2. Reddish Brine Mud Exposures: Patches of reddish brine mud layer (Figure 4) are evident on a slightly elevated dome (referred to here as "the Island Dome") in the 1965 image. This dome experiences seasonal flooding from Lake Karum due to runoff from the Afar margin slopes to the west and the Danakil Alps to the east (Figure 1). While the origin of the reddish brine mud layer remains unclear, its discontinuous exposures on both sides of the YLF show a gradual decrease in size, likely due to erosion.
3. Eroding Plateaus: Two plateaus, measuring 10–15 m in length and 3 m in height, are observed along the northwest-southeast structural trend (Figure 4b). These plateaus, characterized by vertical scarps of undeformed, horizontal salt layers overlain by clays and surrounded by large blocks, have been gradually eroding since 1965. The lack of deformation, either internal or in the surrounding salt flats, suggests that their formation resulted from localized uplift.
4. Persistent Hydrothermal Activity: A 10 × 20 m lake (the "White Lake'), exhibiting intense bubbling in 2019, likely existed in 1965 based on satellite imagery. In 2019, various hydrothermal manifestations were observed in the northern YLF. The White Lake represented the largest hydrothermal fluid body, while numerous smaller pools, some located along the YLF, displayed varying degrees of activity, with some already dry (see Figures 4b–4d). Bubbling, indicative of ongoing hydrothermal activity, was noted in many locations, including active pools, dry pools, and beneath salt plates. Additionally, large depressions within the reddish brine mud layer are interpreted as remnants of former pools or small lakes.

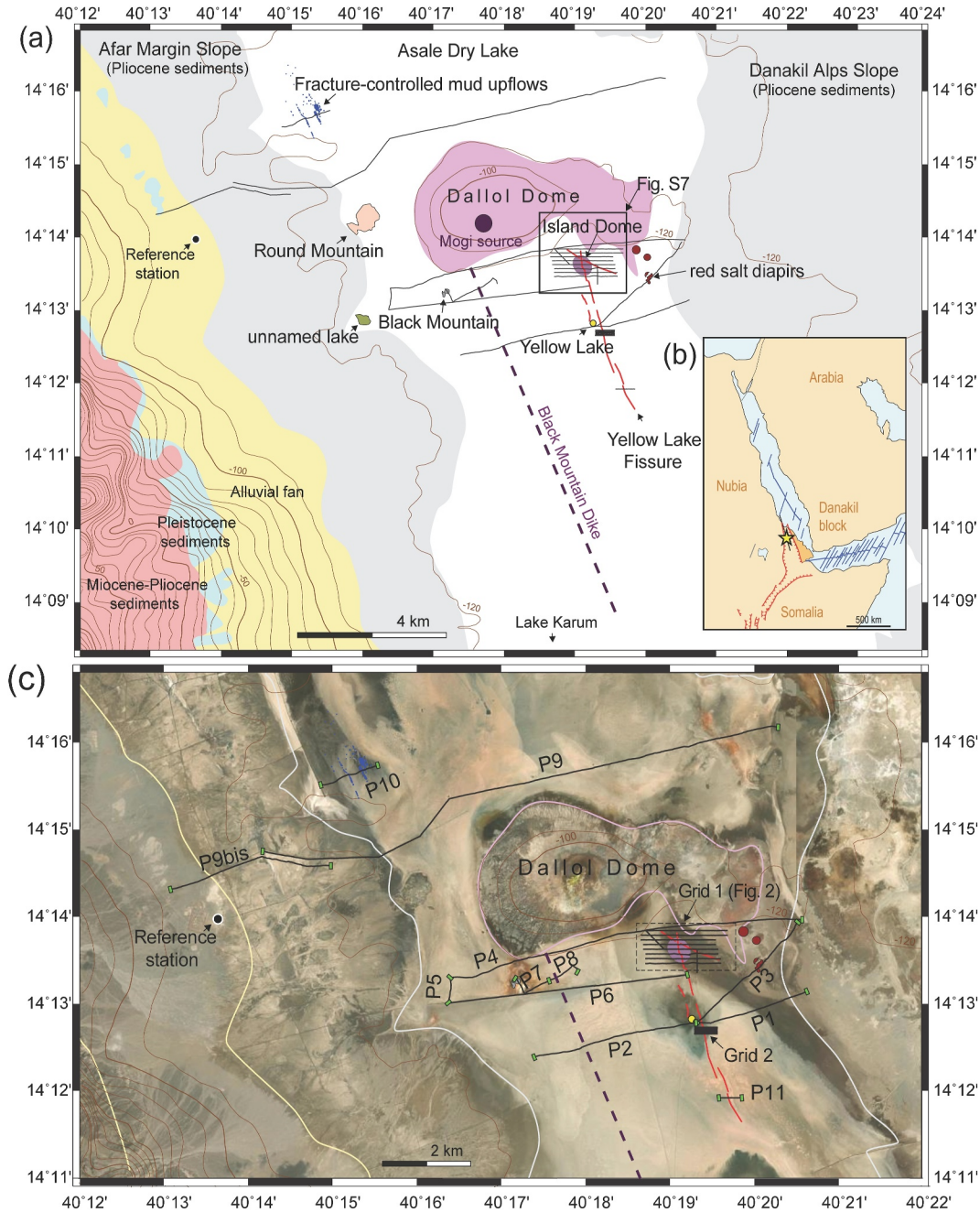

Figure 1. Tectonic framework of the Dallol area, Danakil Depression. (a) Map showing the main tectonic and hydrologic features with locations of Grids 1 and 2 and profiles 1–11. Black solid lines: magnetic data from 2019 field campaign; dashed line: Black Mountain Dike (Nobile et al., 2012). Dallol dome uplift linked to sill emplacement (López-García et al., 2020). Geological data from Hagos et al. (2016); topography from SRTM V3 1-arc DTM (Farr et al., 2007). Black solid box indicates Figure S7 in Supporting Information S1. (b) Major tectonic setting between Africa and Arabian Plate showing northern Afar rift (black), Red Sea and Gulf of Aden spreading ridges (blue), and East African Rift (red). Yellow star indicates the location of the survey area. (c) Magnetic survey lines (P1-P11, Grid 1, Grid 2) superimposed on satellite imagery taken 22 January 2019 (Esri, 2024) of the Dallol Dome area. Black solid lines are magnetic survey track lines and green bars describe the margin of each trackline. For detailed magnetic anomaly information is described in Supporting Information S1 (Figures S2, and S4–S7).

3. Data and Methods

3.1. Survey Data Acquisition

In January 2019, we conducted a geological and magnetic survey across the YLF hydrothermal system South of Dallol using two high-precision GemSystems GSM-19 Overhauser magnetometers. To investigate the magnetic anomalies in Danakil Depression, we acquired data on two gridded areas (Grid 1 and Grid 2) and along 12 individual profiles, for a total survey distance of 78 km (see Figure 1c for details). During our investigation, we placed the magnetic sensor at a distance of 1.8 m above the ground. In the case of Grid 1, covering the main area of active hydrothermal circulation at the YLF, we collected magnetic data along eight East-West parallel profiles 100 m apart and two additional oblique profiles cutting across the East-West profiles to correct the leveling errors. A spacing of 15 m between points was adopted to investigate the effect of hydrothermal manifestations on magnetic anomalies (Grid 1 in Figure 1). The measured magnetic field in the survey area ranges between 37,665 and 37,789 nT. In addition, we present 12 individual magnetic profiles and a smaller grid (Grid 2) that help constrain the magnetic interpretation (see Figures S4 and S5 in Supporting Information S1). Such a magnetic survey offers adequate high resolution to address shallow, near-surface processes.

3.2. Magnetic Data Processing and Correction

To account for temporal variations in the magnetic field, a reference magnetometer was temporarily installed 5 km west of the Dallol dome (location in Figure 1 and Table S1 in Supporting Information S1). We acquired the ambient scalar magnetic field every minute with readings ranging from 37,744 to 37,775 nT, mostly exhibit diurnal variation and potential instrumental errors (Figure S1 in Supporting Information S1). The International Geomagnetic Reference Field model (IGRF) (Alken et al., 2021) indicates an almost constant value of approximately 37,657 nT (with a regular variation of 0.08 nT per day) at the reference station.

To remove potential instrumental errors in the reference magnetometer data, we compared them with the corresponding IGRF value at the same location and time (Figure S1 in Supporting Information S1). This comparison was aimed to identify a linear instrumental drift or a constant offset relative to the stable IGRF baseline. The method for removing this drift and offset varied based on the daily measurement duration. For long measurement days (about 12 hr per day), we fitted the data directly to the IGRF trend. For shorter measurement days, where direct fitting could introduce errors, we applied a normalized diurnal curve (generalized from the long-duration data) and performed leveling by adjusting only a constant value. This process yielded the corrected diurnal variation data (see Figure S1 in Supporting Information S1). This process yielded the corrected diurnal variation data (see Figure S1 in Supporting Information S1). The magnetic anomaly was then derived from the total magnetic field measurements of the mobile station by subtracting this corrected diurnal variation at the time of each mobile measurement. Furthermore, we improved the magnetic anomaly maps for Grid 1 and Grid 2 by performing crossover error analysis (Wessel, 2010) to correct for any offset differences between the profiles at their intersected points.

The final corrected data were compiled using a continuous curvature surface algorithm to produce the magnetic anomaly map with grid cell size of 0.4 arcsec (approx. 12.3 m) in the East-West direction and 3 arcsec (approx. 92.6 m) in the North-South direction. The resulting magnetic anomaly grid map is shown hereafter for Grid 1 (Figure S2a in Supporting Information S1).

3.3. GPS Data and Correction

The GPS data, with a horizontal accuracy of 3 m, were collected for each magnetic measurement point. Topographic variations along Grid 1 were estimated using both a Pleiades digital terrain model derived from UAV images (Mège et al., 2023) and GPS data. Although the vertical accuracy of GPS measurements is poor, both methods yield similar elevation variations (see Figures S8 and S9 in Supporting Information S1). The satellite topography model from Pleiades, being more quantitatively constrained, is considered to provide a more reliable vertical amplitude variation.

3.4. Magnetic Anomaly Data Analysis

To separate anomalies originating from sources at different depths, we investigated the different wavelengths of the measured magnetic anomalies by progressively analyzing then removing the longer wavelengths, first analyzing the full spectral content (Figure 2a) on the few long profiles crossing the rift valley, then by applying a

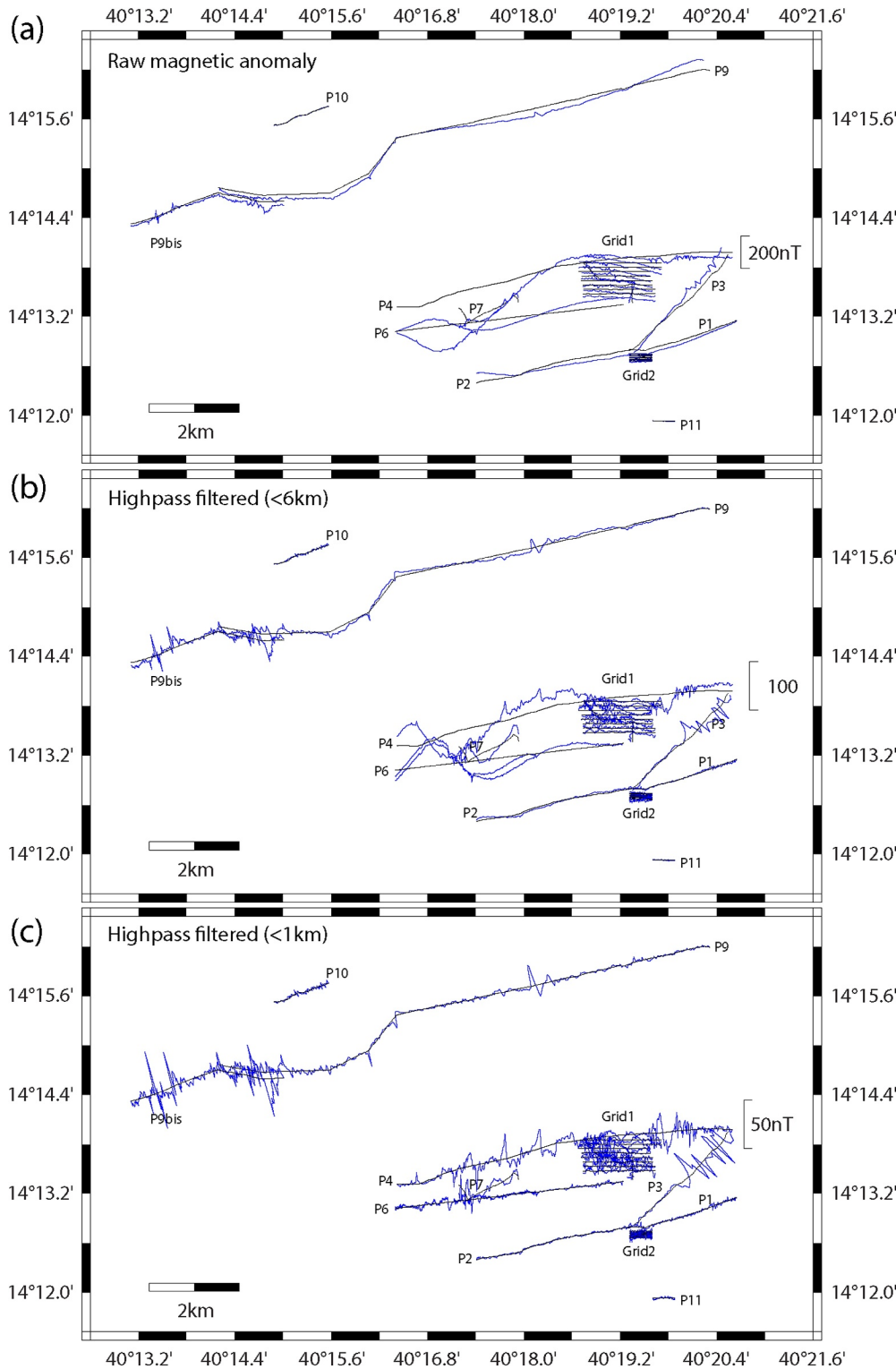

Figure 2. Magnetic anomaly profiles across the study area. (a) Comparison between raw magnetic anomalies and high-pass filtered magnetic anomalies ((b) <6 km; (c) <1 km). Blue wiggles indicate the magnetic anomalies and black solid lines indicate the survey track.

6-km high-pass filter along the tracks (Figure 2b) to observe the intermediate wavelength content, then by applying a 1-km high-pass filter along the tracks (Figure 2c) to enhance the shortest wavelength content.

For the dense survey grids (Grids 1 and 2), a different approach was used to isolate the target anomalies. We removed a first-order regional trend from the final corrected magnetic anomaly maps (see Figures S2 and S4 in Supporting Information S1). This detrending method was chosen specifically to preserve the weak-amplitude, short-wavelength anomalies generated by the shallow magnetized mud layer.

Magnetic data acquisition was complemented by field observations and satellite imagery data. Geological observations in 2018 and 2019 provided evidence of ongoing hydrothermal activity, crucial for interpreting the magnetic anomalies, as inferred from the morphology and hydrology of small pools (typically <1 m in diameter), observations of hydrothermal fluid bubbling, and acoustic effects of shallow subsurface bubbling underneath salt plates around the magnetic data points (Figure 4). We used the geological information to constrain further the relationships between geology and magnetic anomalies. Satellite images, spanning 1965–2023, were used to understand the evolution of the hydrothermal site. The high-resolution Planetscope and Pleiades images from January 2019 helped characterize the surface geology during the magnetic survey.

We further validated our interpretations by constructing simple 2D magnetic models along selected Grid 1 profiles (Figure 5). These models, based on Talwani and Heirtzler (1964), assume a geometry and magnetic susceptibility for magnetized bodies, allowing us to compare synthetic and observed magnetic anomalies.

4. Results

In the main study area (Grid 1), the magnetic anomalies range between −8 and 151 nT (Figure S2a in Supporting Information S1), and the detrended residual magnetic anomalies range between −38 and 26 nT (Figure 3c and Figure S2c in Supporting Information S1).

Our analysis of the magnetic data revealed systematic long-wavelength anomalies in each profile (see the total magnetic anomaly presented in Figure 2a and Figure S2a in Supporting Information S1). These anomalies, characterized by wavelengths typically exceeding 6 km and amplitudes on the order of 124 nT, are particularly prominent in the Grid 1 area. As illustrated in Figure S2a in Supporting Information S1, these long-wavelength components dominate the total magnetic field and likely reflect deeper tectonic and magmatic structures, resemble those described by Holwerda and Hutchinson (1968). A strong magnetic high is observed southeast of the Dallol Dome on Profile P4 and on Grid 1, whereas a strong magnetic low appears south of the Dome. This signal attenuates with distance from the Dome, with only weak anomalies on profile P2 further south and no anomaly on profile P9 further north (Figure 2a).

Focusing on the dense survey of Grid 1, a weak wide positive magnetic anomaly (∼8 nT) is observed over the area covered with the reddish brine mud layer, corresponding to the Island Dome (black dashed line on Figure 3c). This anomaly extends beyond the limits of the Island Dome (gray dashed line on Figure 3c) and fades away. Other smaller positive anomalies are observed locally without being associated with any recognized geological feature, the biggest being observed around N14° 13′ 51″, E40° 19′ 22″. Conversely, small (∼50 m) magnetic anomaly lows are observed over the YLF and other fissures, as well as over the hydrothermal pools and other bubbling areas. Removing first order trend from long wavelengths isolates these anomalies (Figure 3c and Figure S2c in Supporting Information S1).

Additional magnetic data acquired in the area during the 2019 campaign show that Grid 2, a smaller magnetic anomaly grid in the Yellow Lake area (Figure 1) that cuts across the YLF and adjacent fissures, displays a weak positive magnetic anomaly (∼2–3 nT) after detrending along the strike of the fissure near surficial mud patches (See Figure S4c in Supporting Information S1 and Figure 5d). In contrast, Profiles 1, 2 and 3, which cut across the YLF between Grid 1 and Grid 2 (Figure S6a in Supporting Information S1), and Profile 11 acquired in the south of Grid 2, do not exhibit any magnetic anomaly (Figure S6b in Supporting Information S1).

Only three areas show noticeable short wavelength magnetic anomalies as depicted by the 6 and 1 km- high-pass filtered additional magnetic profiles (Figure 2). Profile 9 northwest of the Dallol Dome cuts across the lower part of the debris slope marking the western border of the rift, and the observed anomalies (maximal amplitude of 50 nT) probably reflect the presence of fallen magnetized blocks at a shallow depth. Profiles 4 to 8 have been acquired in the close vicinity of the southern end of the Dallol Dome, and the decreasing amplitude of the observed anomalies

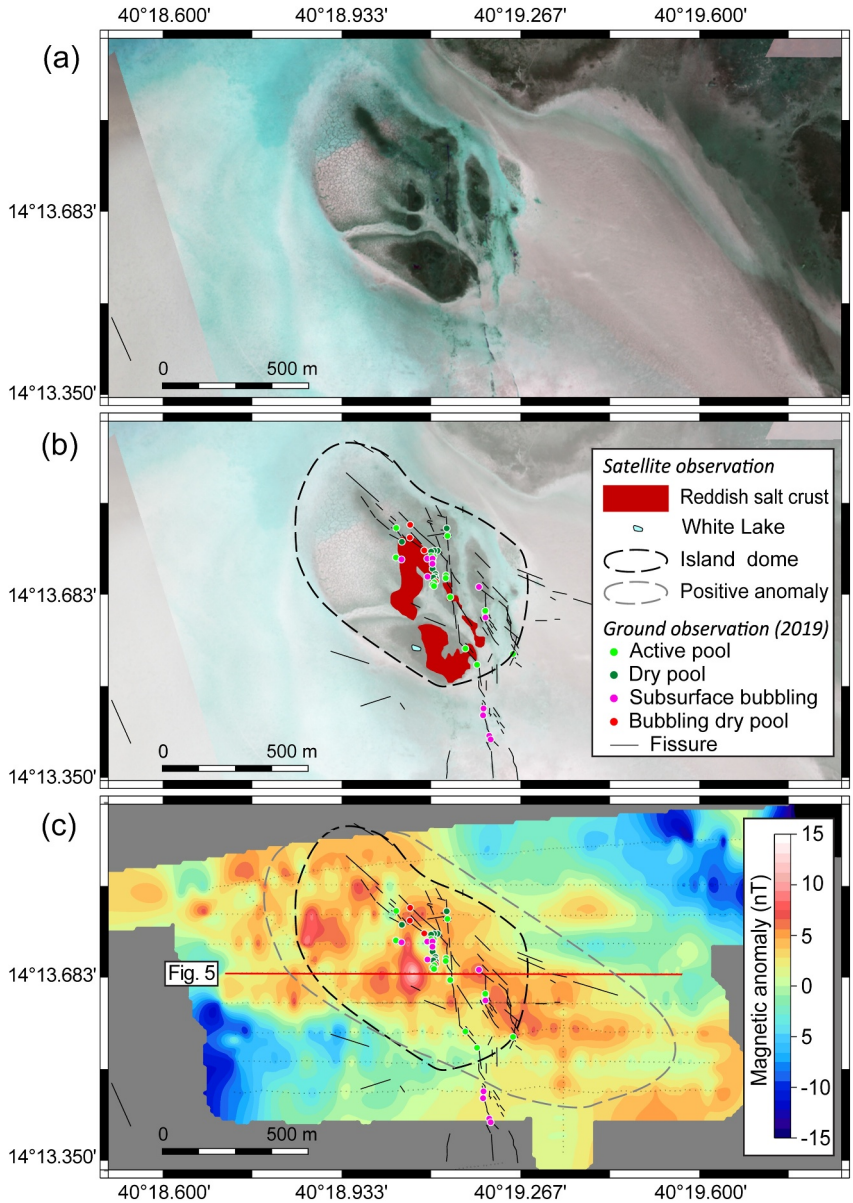

Figure 3. Magnetic and geological characterization of Grid 1, northern YLF area. (a) Pleiades1B satellite imagery (26 February 2019; see Table S2 in Supporting Information S1). (b) Surface geology map highlighting hydrothermal features from satellite and ground observations. (c) Short-wavelength (<1.5 km) magnetic anomaly map from Grid 1 after detrending. The black dashed contour shows Island dome; the gray dashed contour indicates the potential extent of the magnetized reddish brine mud layer; black dotted lines represent magnetic survey tracks.

southward (from a maximal amplitude of 100 nT on Profile 4–50 nT on Profile 6) probably reflects the progressive deepening of the dome beneath the recent evaporitic sediment covers. Finally, distinct anomalies (maximal amplitude of 40 nT) are observed east of the main survey area (Grid 1) on Profiles 3 and 4, where a hill-like structure composed of interbedded salt and thick, magnetized mud layers was observed in the field (Figures 5e and 5f).

5. Discussion

5.1. Magnetic Anomalies and Tectonic-Hydrothermal Interactions

The long-wavelength anomalies observed in our study area provide insights into deeper tectonic structures. Nobile et al. (2012) proposed the existence of a dike, approximately 2 km deep and 1–2 m thick, intruding from

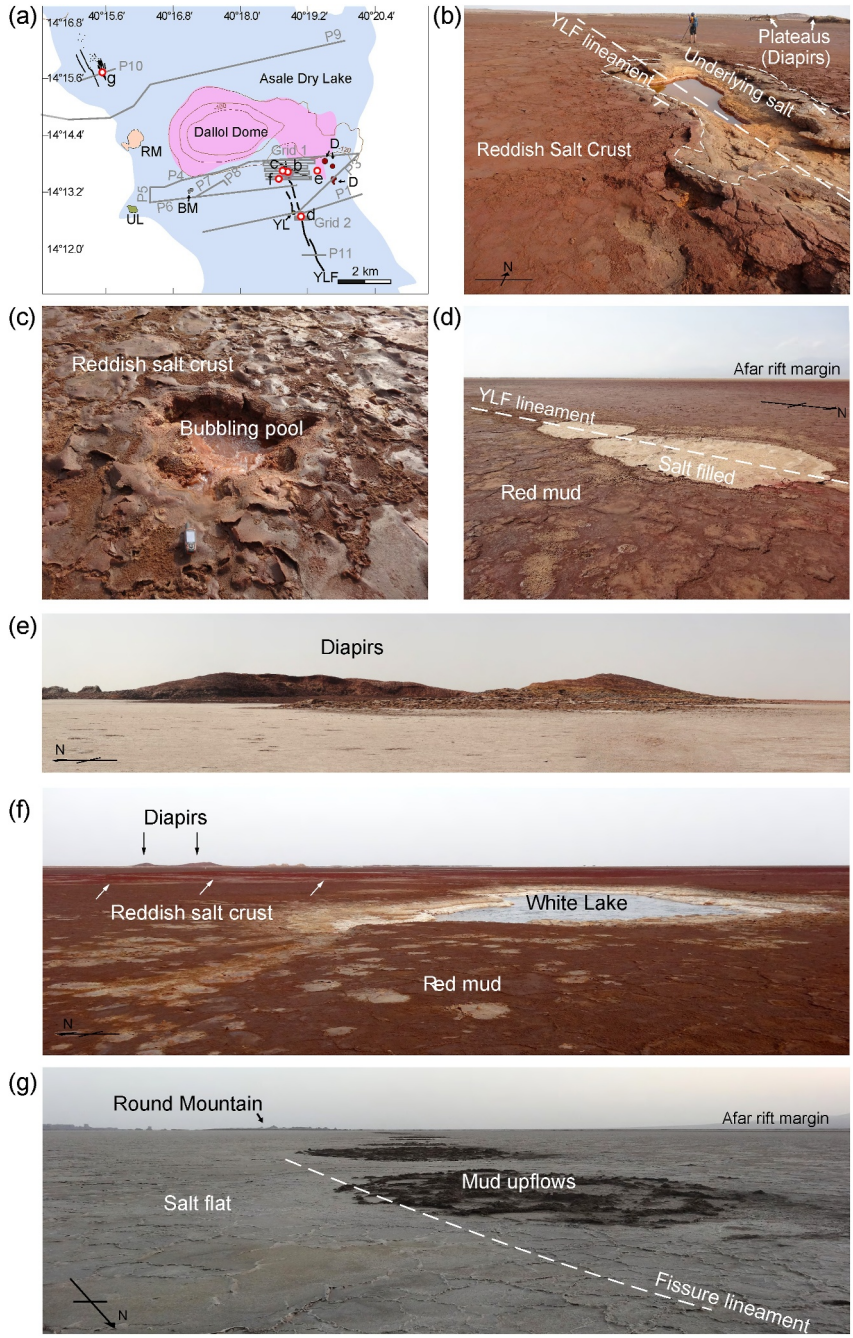

Figure 4. Hydrothermal manifestations of incipient rifting in the Dallol area. Surface features demonstrate active hydrothermal circulation along structural features. (a) Location map with photograph sites (red dots). (b)–(d) Bubbling saline pools along Yellow Lake Fissure (YLF). (e) Uplifted interbedded reddish mud and salt on salt flat. (f) Bubbling white lake adjacent to YLF. (g) Hydrothermal mud upflows along fissure trace. BM, Black Mountain; D, uplifted structure; FU, Fissure upflows; RM, Round Mountain; UL, Unnamed lake; YL, Yellow Lake; YLF, Yellow Lake Fissure.

the southwest of the Dallol Dome in a N20°W direction, toward the Erta'Ale volcano. While magmatic dikes typically produce strong magnetic anomalies due to their mafic mineral content, our observed long-wavelength anomalies do not show the characteristic 2-D signature of a dike. We hypothesize that the long wavelength anomaly may be affected by multiple stacked older dikes within the underlying basement whose combined effects create the observed anomalies. Such a scenario is geologically plausible within a rift zone having experienced repeated episodes of magmatism over time (Ferguson et al., 2010; Moore et al., 2021).

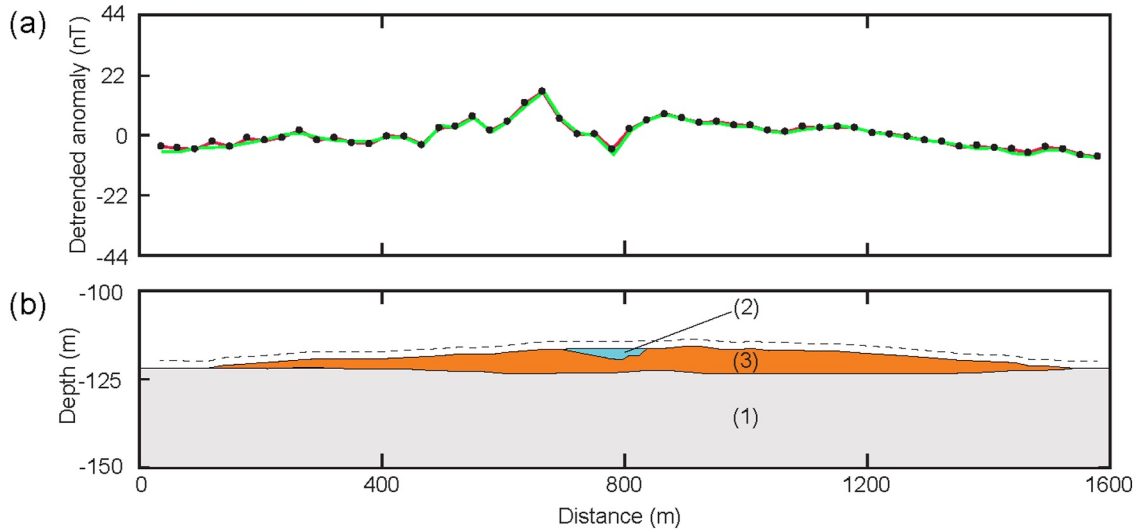

Figure 5. Two-dimensional magnetic profile across the Island Dome. Observed and modeled magnetic signatures with interpreted subsurface structure. (a) Magnetic anomaly profile showing measurements (black dots), observed profile (red line) and computed anomaly (green line) along profile 4 of Grid 1. (b) Interpreted cross-section showing non-magnetic layers (1) (gray), altered reddish brine mud layer (2) (blue, 0.03 SI apparent susceptibility) and reddish brine mud layer (3) (orange, 0.1 SI apparent susceptibility). The black dashed line represents the observation height of 1.8 m. Vertical exaggeration is 6.

Further analyzing the magnetic anomalies associated to the Island Dome with satellite imagery and our field observations (see Figures 3 and 4), we conclude that these anomalies are better explained by the presence of a magnetized layer within the island and the surrounding area. The observed anomalies characterized with a weak and broad positive amplitude and its sharp transitions at the center of the fissure, suggesting a tabular magnetized mud layer at the surface perturbed by narrow hydrothermal manifestation at the center.

The multiple short-wavelength wiggles superimposed on the positive anomaly indicate local physical and chemical heterogeneities within the reddish mud and reflect subtle surficial changes. We observed this phenomenon distinctly across the YLF, where the wiggles are more prominent in the West than in the East (Figure 3c). The western side is relatively dry, with a developed thick reddish mud structure. On this side, we consider that complex magnetization structures from past hydrothermal deposition were preserved. The subsequent rapid salt crystallization not only locked in this signature but also likely caused extensive micro-fracturing of the brittle magnetized layer, creating the observed wiggles. In contrast, the eastern side is covered with wet mud and has relatively flat magnetic features, suggesting that ongoing hydrothermal activity and flood-induced redeposition have continuously altered and homogenized the magnetic properties.

The geographical correspondence between the positive anomaly and the reddish brine mud layer exposures suggests that the latter is the most likely source of the observed anomalies and probably bears a magnetic mineral such as hematite or magnetite. The anomaly lows observed over the hydrothermal manifestations reflects the chemical alteration of this mineral or the mechanical disruption of the layer following the hydrothermal fluid circulation and the formation of fissures, ponds, or other hydrothermal features.

5.2. 2-D Forward Modeling Analysis

Forward modeling offers an easy way to confirm this interpretation (Figure 5). For simplicity, we assume only three types of magnetic bodies in our study area: (a) a magnetized layer following the topography, (b) an altered magnetized layer affected by hydrothermal activity, and (c) a non-magnetic underlying basement, as the short wavelength of the investigated anomalies prevents any deeper sources to play a significant role. The surface topography for the model was constrained by DTM of satellite and UAV (Figure S8 in Supporting Information S1), and GPS observations (Figure S9 in Supporting Information S1). We assume an apparent magnetic susceptibility of 0.1 SI for layer (1) and adjust the interface between layers (1) and (3) to fit the observed anomalies over most of the profile. Since layer (2) is considered an altered part of layer (1), its base was defined by interpolating the bottom surface of layer (1) across the altered zone, and finally adjust the magnetic susceptibility of layer (2) to fit the observed anomalies over the YLF. The relatively high SI value of 0.1 used in layer (1) is

plausible due to the formation of magnetite from iron-rich rocks originating from magma intrusion that underwent hydrothermal alteration (Lamadrid et al., 2017; Simon et al., 2004). This process may have introduced a significant amount of magnetite into the hydrothermal fluids, which, according to Kotopoulou et al. (2019), can contain up to 150 g/L of iron, along with the surrounding salt in the Dallol hydrothermal system. These iron-rich fluids eventually upwell through fissures to form the reddish mud layer. Therefore, the strong magnetic anomaly is likely a combined effect between the high induced magnetization and a significant Natural Remanent Magnetization (NRM) acquired during the deposition. This can be quantified by the relationship between apparent susceptibility (S_{app}), true susceptibility (S_{true}), and NRM, which is defined as $S_{app} = S_{true} + \mathrm{NRM}/H$. Rearranging this gives $\mathrm{NRM} = (S_{app} - S_{true}) \cdot H$. Applying this equation, if we assume the background magnetic field of the area (H) is 37,660 nT (approximately 30 A/m) and the true susceptibility of this mud layer is a plausible 0.03 SI, the NRM of 2.1 A/m in a direction parallel to the ambient magnetic field could sufficiently explain the apparent susceptibility of 0.1 SI used in our model.

Due to the lack of samples, we could not measure the NRM, and for modeling simplicity, its effect is implicitly included in the apparent susceptibility value. The initial, somehow arbitrary value of magnetic susceptibility that we adopted will be modified once samples can be collected and their magnetic properties measured, something that unstable political conditions prevents at the time this paper is written. It is worth noting that a change in this parameter will modify the depth of the interface between (1) and (3) but will not affect the results of this study. The modeled anomaly fits the observed one and shows that our interpretation is reasonable within the available geological information.

5.3. Two Possible Scenarios for the Formation of Surface Magnetization

Before samples are collected to further investigate the emplacement of the reddish mud layer, we can only speculate on the two following scenarios to explain the magnetic contrast associated with the Island Dome.

The first possibility is that the magnetized layer responsible for the anomaly is limited to the Island Dome itself. This layer would have formed by local reddish mud eruption from a proto-YLF in response to underlying hydrothermal circulation. Hydrothermal fluids bearing large quantities of ferric and sulfide minerals are frequently vented along the fissure, and their continuous deposition resulted in the development of thick layers of magnetized muds and associated sulfide minerals around the vent site. The periodic brine inflow from the southern lake was trapped in the Danakil Depression and created a temporary, calm, and shallow water environment and mixing with hydrothermal fluids during this period. During these flooding events, the orientation of magnetic minerals parallels to the Earth's magnetic field in the lake environment, resulting in forming a coherent Natural Remanent Magnetization (NRM). Then, the extremely arid climate of this region causes the rapid evaporation of trapped water, facilitating the acquisition and preservation of a consistent remanent magnetization in the magnetized mud. Also, the inherent magnetic susceptibility of the magnetic minerals would lead to the observation of a high scalar magnetic anomaly.

A second possibility is that the magnetized layer extends deeper beyond the study area and shallows under the Island Dome, possibly as the result of limited salt diapirism in this area, preserving coherent magnetization—a more mature diapir would have generated complex deformation and the loss of the magnetized layer coherency. The deeper part of the layer beyond the Island Dome would not have any significant magnetic effect, considering its weak magnetization contrast and the short wavelengths considered in our study.

In the vicinity of fissures with active hydrothermal circulation, the original magnetic signature is weakened by two concurrent mechanisms. First, vigorous fluid flow mechanically disrupts the layer, causing a random orientation of magnetic minerals that destroys the coherent NRM. Second, hydrothermal fluids promote chemical alteration, such as the oxidation of magnetite to less-magnetic hematite. This alteration not only aids in destroying the NRM but also crucially lowers the intrinsic bulk susceptibility of the material itself. Consequently, as the NRM is eliminated and the intrinsic susceptibility is chemically reduced, the apparent susceptibility of these altered zones converges to this new, lower value, such as the 0.03 SI used in our model.

5.4. Formation and Implications of the Reddish Mud Layer

Active magmatism in the East African Rift Valley drives thermal instability in the surrounding salt layers, promoting dehydration reactions and the formation of highly acidic brines (Figure 5a). This brine acidity results

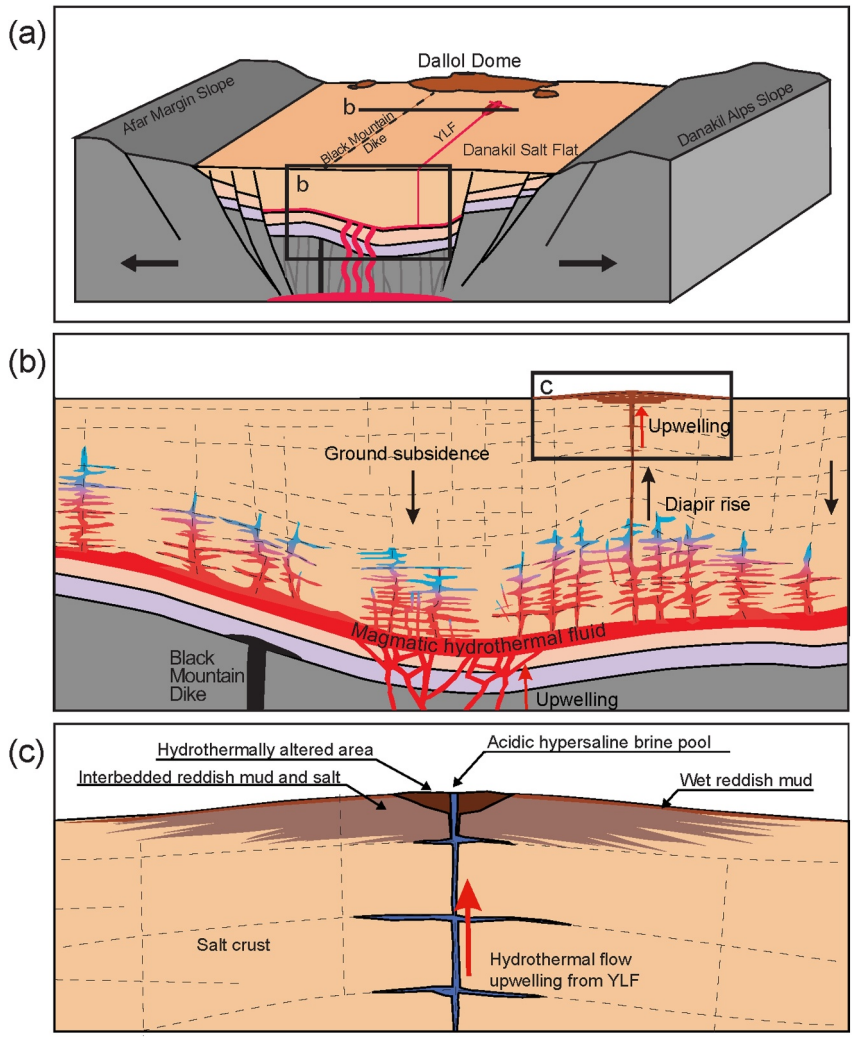

Figure 6. Schematic illustration of the YLF hydrothermal system. (a) Three-dimensional schematic of the Dallol area, highlighting the YLF fault system and the Island Dome. The YLF is a north-south fault zone traversing the Danakil salt flat. (b) Cross-sectional representation of the YLF, modified from Otálora et al. (2022), illustrating a possible origin of the reddish brine mud layer. Hydrothermal fluids rise through the YLF and erupt as brine muds, which dry to form a magnetized crust. (c) Detailed cross-section showing the interaction of hydrothermal fluids with the reddish mud layer along the YLF. This process reduces the magnetization in the altered zone, producing a weak negative magnetic anomaly, while the relatively undisturbed mud layers generate weak positive anomalies. The hypersaline brine pool at the surface, characterized by low pH, reflects intense hydrothermal activity.

from the thermal decomposition of salt minerals and interaction with magmatically derived hydrothermal fluids (Otálora et al., 2022). Magmatic activity and tensional stresses within the rift, combined with localized diapiric uplift by deep thermal convection (Talbot, 1978), facilitate the formation of the YLF and within these thick (>1 km) salt layers (Hayward & Ebinger, 1996). This uplift also plays an important role in creating the broad, gentle dome-like topography along the YLF. This fracture system may serve as the primary conduit for the ascent of magmatic hydrothermal fluids toward the surface (Figure 6b).

Magnetite within these ascending fluids precipitates near the surface in a partially oxidized state due to the oxygen-poor hydrothermal environment (Simon et al., 2004). Subsequent exposure to highly acidic brines and the atmosphere leads to further oxidation, transforming magnetite into hematite, a mineral with weaker magnetic properties. As hematite is a dominant component of the Red Salt (Otálora et al., 2022), these mineralogical transformations are likely responsible for the formation of the reddish brine mud layers and sediments observed on the surface around the YLF (Figure 6c).

These observations confirm that the outcropping or shallow reddish brine mud layer, rich in primary magnetite, is the source of the observed positive magnetic anomalies. The YLF is not associated with a magnetic anomaly along all its length but only in the Island Dome area. This implies that if the reddish crust originated from a mud eruption, this eruption should be limited to the Island Dome and vicinity area. The flat area that characterizes the floor of the Asale dry lake is devoid of any significant magnetic signal, as expected in an area where sedimentation is controlled by recent evaporitic processes. This spatial variability is also evident in Grid 2 (Figure 4c). The positive anomaly along the YLF is considerably subtler than in Grid 1, reflecting both weaker hydrothermal activity and a reduced volume of the interbedded mud and salt layers.

6. Conclusion

Through a detailed high-resolution magnetic investigation of the Dallol area, Ethiopia, our study provides new insights into the magnetic signatures of hydrothermal systems in volcanic-evaporitic environments. We identified the surficial reddish brine mud layer as the most likely primary magnetized layer, generating weak positive magnetic anomalies (∼7 nT), while active hydrothermal manifestations create distinct magnetic lows (∼20 nT) by weakening this magnetization through mechanical disruption and chemical alteration.

These findings suggest that hydrothermal activity may consistently results in magnetization loss when acting upon a magnetized substrate, whether through mechanical destruction or chemical alteration. This pattern aligns with observations from basalt-hosted hydrothermal systems at mid-ocean ridges (Szitkar, Dyment, Choi, & Fouquet, 2014; M. A. Tivey & Dyment, 2010; M. A. Tivey et al., 1993), suggesting a common mechanism across diverse geological settings, from volcanic-evaporitic environments to mid-ocean ridges. Additionally, our study supports that detailed investigations of hydrothermal systems can be successfully conducted in accessible continental settings, providing unique insights that complement studies from less accessible environments like deep-sea hydrothermal vents.

In particular, the implications of our findings extend beyond the Dallol area, with important applications for understanding hydrothermal fluid circulation in divergent plate boundaries and monitoring the evolution of hydrothermal systems. The relationship between magnetic anomalies and fluid circulation provides a valuable tool for studying heat transfer mechanisms and fluid-rock interactions in the crust, with broad implications for both fundamental research and practical applications such as geothermal resource exploration and volcanic hazard assessment.

While this study provides valuable insights into the magnetic signatures of hydrothermal systems in a volcanic-evaporitic environment, the lack of direct sample analysis limits our understanding of the precise magnetic mineralogy and magnetization values of the reddish brine mud layer. Future work should focus on sample acquisition and analysis, coupled with integrated geophysical and geochemical studies, to further refine our models and explore the general applicability of these findings to similar settings.

Conflict of Interest

The authors declare no conflicts of interest relevant to this study.

Data Availability Statement

All new data presented in this manuscript are openly accessible on Zenodo under the citation Choe et al. (2025), available at https://zenodo.org/records/13845616.

Acknowledgments
We thank Fabio Caratori Tontini and Marta Neres for corrections and constructive comments on the manuscript. We also appreciate the editor Mark Dekkers. Field work was supported by Europlanet 2020 RI (EU Horizon 2020, Grant 654208), and laboratory work (DM) by the EXOMHYDR project (TEAM program, Foundation for Polish Science, co-financed by the European Regional Development Fund) and a Polish Academy of Sciences-CNRS fellowship at Institut de physique du globe de Paris. HJ acknowledges support from the NRF of Korea's Sejong Science Fellowship (NRF-2021R1C1C2003742), Basic Research Laboratory (NRF-2022R1A4A3027001), and G-LAMP project (RS-2023-00301938), and KIMST funded by the Ministry of Oceans and Fisheries (RS-2023-00259686). UAV topography data were provided by Pascal Allemand (2018 field campaign, Mège et al., 2023). We thank Vincent Lesur and IPGP magnetic observatories for the use of high-precision GemSystems GSM-19 Overhauser magnetometers.

References

Albino, F., & Biggs, J. (2021). Magmatic processes in the East African Rift System: Insights from a 2015–2020 Sentinel-1 InSAR survey. *Geochemistry, Geophysics, Geosystems*, *22*(3), e2020GC009488. https://doi.org/10.1029/2020GC009488

Alken, P., Thébault, E., Beggan, C. D., Amit, H., Aubert, J., Baerenzung, J., et al. (2021). International geomagnetic reference field: The thirteenth generation. *Earth Planets and Space*, *73*(1), 49. https://doi.org/10.1186/s40623-020-01288-x

Alt, J. C. (1995). Subseafloor processes in mid-ocean ridge hydrothennal systems. In S. E. Humphris, R. A. Zierenberg, L. S. Mullineaux, & R. E. Thomson (Eds.), *Seafloor hydrothermal systems: Physical, chemical, biological, and geological interactions*. https://doi.org/10.1029/GM091p0085

Bastow, I. D., Booth, A. D., Corti, G., Keir, D., Magee, C., Jackson, C. A.-L., et al. (2018). The development of late-stage continental breakup: Seismic reflection and borehole evidence from the Danakil Depression, Ethiopia. *Tectonics*, *37*(9), 2848–2862. https://doi.org/10.1029/2017TC004798

Belilla, J., Iniesto, M., Moreira, D., Benzerara, K., López-García, J. M., López-Archilla, A. I., et al. (2021). Archaeal overdominance close to life-limiting conditions in geothermally influenced hypersaline lakes at the Danakil Depression, Ethiopia. *Environmental Microbiology*, *23*(11), 7168–7182. https://doi.org/10.1111/1462-2920.15771

Carniel, R., Jolis, E. M., & Jones, J. (2010). A geophysical multi-parametric analysis of hydrothermal activity at Dallol, Ethiopia. *Journal of African Earth Sciences*, *58*(5), 812–819. https://doi.org/10.1016/j.jafrearsci.2010.02.005

Cavalazzi, B., Barbieri, R., Gómez, F., Capaccioni, B., Olsson-Francis, K., Pondrelli, M., et al. (2019). The Dallol Geothermal Area, Northern Afar (Ethiopia)-an exceptional planetary field analog on Earth. *Astrobiology*, *19*(4), 553–578. https://doi.org/10.1089/ast.2018.1926

Choe, H., & Dyment, J. (2020). Decreasing magnetization, lithospheric flexure, and rejuvenated hydrothermalism off the Japan-Kuril subduction zone. *Geophysical Research Letters*, *47*(9), e2019GL085975. https://doi.org/10.1029/2019GL085975

Choe, H., & Dyment, J. (2021). The fate of marine magnetic anomaly in subduction zones: A global appraisal. *Earth and Planetary Science Letters*, *561*, 116787. https://doi.org/10.1016/j.epsl.2021.116787

Choe, H., Dyment, J., & Mège, D. (2025). *(Magnetic dataset) high-resolution magnetic investigation of a hydrothermal system in a volcanic-evaporitic environment*. Zenodo. Retrieved from https://zenodo.org/records/13845616

Cox, S. F. (2005). Coupling between deformation, fluid pressures, and fluid flow in ore-producing hydrothermal systems at depth in the crust. In J. W. Hedenquist, et al. (Eds.), *One Hundredth anniversary volume* (pp. 59–72). Society of Economic Geologists. https://doi.org/10.5382/AV100.04

Esri. (2024). Satellite imagery. Retrieved from https://www.esri.com

Farr, T. G., Rosen, P. A., Caro, E., Crippen, R., Duren, R., Hensley, S., et al. (2007). The shuttle radar topography mission. *Review of Geophysics*, *45*(2), RG2004. https://doi.org/10.1029/2005RG000183

Ferguson, D. J., Barnie, T. D., Pyle, D. M., Oppenheimer, C., Yirgu, G., Lewi, E., et al. (2010). Recent rift-related volcanism in Afar, Ethiopia. *Earth and Planetary Science Letters*, *292*(3–4), 409–418. https://doi.org/10.1016/j.epsl.2010.02.010

Franzson, H., Helgadóttir, H. M., & Óskarsson, F. (2015). Surface exploration and first conceptual model of the Dallol Geothermal area, northern Afar, Ethiopia. In *Proceedings of the World Geothermal Congress* (Vol. 2015, p. 11043).

Hagos, M., Konka, B., & Amed, J. (2016). A preliminary geological and generalized stratigraphy of western margin of northern Afar depression, Dallol Area, northern Ethiopia. *Momona Ethiopian Journal of Science*, *8*, 1–22. https://doi.org/10.4314/mejs.v8i1.1

Hayward, N. J., & Ebinger, C. J. (1996). Variations in the along-axis segmentation of the Afar Rift system. *Tectonics*, *15*(2), 244–257. https://doi.org/10.1029/95TC02292

Heap, M., Baumann, T., Gilg, H. A., Kolzenburg, S., Ryan, A. G., Villeneuve, M., et al. (2021). Hydrothermal alteration can result in pore pressurization and volcano instability. *Geology*, *49*(11), 1348–1352. https://doi.org/10.1130/G49063.1

Holwerda, J. G., & Hutchinson, R. W. (1968). Potash-bearing evaporates in the Danakil area, Ethiopia. *Economic Geology*, *63*(2), 124–150. https://doi.org/10.2113/gsecongeo.63.2.124

Hurman, G. L., Keir, D., Bull, J. M., McNeill, L. C., Booth, A. D., & Bastow, I. D. (2023). Quantitative analysis of faulting in the Danakil Depression Rift of Afar: The importance of faulting in the final stages of magma-rich rifting. *Tectonics*, *42*(6), e2022TC007607. https://doi.org/10.1029/2022TC007607

Illsley-Kemp, F., Keir, D., Bull, J. M., Gernon, T. M., Ebinger, C., Ayele, A., et al. (2018). Seismicity during continental breakup in the Red Sea rift of Northern Afar. *Journal of Geophysical Research: Solid Earth*, *123*(3), 2345–2362. https://doi.org/10.1002/2017JB014902

Kotopoulou, E., Huertas, A. D., Garcia-Ruiz, J. M., Dominguez-Vera, J. M., Lopez-Garcia, J. M., Guerra-Tschuschke, I., & Rull, F. (2019). A polyextreme hydrothermal system controlled by iron: The case of Dallol at the Afar Triangle. *ACS Earth and Space Chemistry*, *3*(1), 90–99. https://doi.org/10.1021/acsearthspacechem.8b00141

Lamadrid, H. M., Rimstidt, J. D., Schwarzenbach, E. M., Klein, F., Ulrich, S., Dolocan, A., & Bodnar, R. J. (2017). Effect of water activity on rates of serpentinization of olivine. *Nature Communications*, *8*(1), 16107. https://doi.org/10.1038/ncomms16107

La Rosa, A., Raggiunti, M., Pagli, C., Keir, D., Wang, H., & Ayele, A. (2023). Extensional earthquakes in the absence of magma in northern Afar: Insights from InSAR. *Geophysical Research Letters*, *50*(10), e2023GL102826. https://doi.org/10.1029/2023GL102826

Le Gall, B., Leleu, S., Pik, R., Jourdan, F., Chazot, G., Ayalew, D., et al. (2018). The Red Beds series in the Erta Ale segment, North Afar. Evidence for a 6 Ma-old post-rift basin prior to continental rupturing. *Tectonophysics*, *747–748*, 373–389. https://doi.org/10.1016/j.tecto.2018.10.002

Lister, C. R. B. (1972). On the thermal balance of a mid-ocean ridge. *Geophysical Journal International*, *26*(5), 515–535. https://doi.org/10.1111/j.1365-246X.1972.tb05766.x

López-García, J. M., Moreira, D., Benzerara, K., Grunewald, O., & López-García, P. (2020). Origin and evolution of the halo-volcanic complex of Dallol: Proto-volcanism in Northern Afar (Ethiopia). *Frontiers in Earth Science*, *17*, 00351. https://doi.org/10.3389/feart.2019.00351

Lutz, R. A., & Kennish, M. J. (1993). Ecology of deep-sea hydrothermal vent communities: A review. *Review of Geophysics*, *31*(3), 211–242. https://doi.org/10.1029/93RG01280

Mège, D., Hauber, E., Dyment, J., Allemand, P., Moors, H., Craen, M. D., & Choe, H. (2023). Tectonic and hydrothermal activity at the Yellow Lake fissure in response to the 2004 Dallol dyke intrusion event in Afar. *Frontiers in Earth Science*, *11*, 1250702. https://doi.org/10.3389/feart.2023.1250702

Moore, C., Wright, T. J., & Hooper, A. (2021). Rift focusing and magmatism during late-stage rifting in Afar. *Journal of Geophysical Research: Solid Earth*, *126*(10), e2020JB021542. https://doi.org/10.1029/2020JB021542

Nobile, A., Pagli, C., Keir, D., Wright, T. J., Ayele, A., Ruch, J., & Acocella, V. (2012). Dike-fault interaction during the 2004 Dallol intrusion at the northern edge of the Erta Ale Ridge (Afar, Ethiopia). *Geophysical Research Letters*, *39*(19), L19305. https://doi.org/10.1029/2012GL053152

Ogubazghi, G., Ghebreab, W., & Havskov, J. (2004). Some features of the 1993 Bada earthquake swarm of southeastern Eritrea. *Journal of African Earth Sciences*, *38*(2), 135–143. https://doi.org/10.1016/j.jafrearsci.2003.12.002

Otálora, F., Palero, F., Papaslioti, E.-M., & Garcia-Ruiz, J. M. (2022). Mineralochemical Mechanism for the formation of Salt Volcanoes: The Case of Mount Dallol (Afar Triangle, Ethiopia). *ACS Earth and Space Chemistry*, *6*(12), 2767–2778. https://doi.org/10.1021/acsearthspacechem.2c00075

Pereira, M. L., Zanon, V., Fernandes, I., Pappalardo, L., & Viveiros, F. (2024). Hydrothermal alteration and physical and mechanical properties of rocks in a volcanic environment: A review. *Earth-Science Reviews*, *252*, 104754. https://doi.org/10.1016/j.earscirev.2024.104754

Scott, S. W., Covell, C., Júlíusson, E., Valfells, Á., Newson, J., Hrafnkelsson, B., et al. (2019). A probabilistic geologic model of the Krafla geothermal system constrained by gravimetric data. *Geothermal Energy*, *7*(1), 29. https://doi.org/10.1186/s40517-019-0143-6

Sibson, R. H. (1996). Structural permeability of fluid-driven fault-fracture meshes. *Journal of Structural Geology*, *18*(8), 1031–1042. https://doi.org/10.1016/0191-8141(96)00032-6

Simon, A. C., Pettke, T., Candela, P. A., Piccoli, P. M., & Heinrich, C. A. (2004). Magnetite solubility and iron transport in magmatic-hydrothermal environments. *Geochimica et Cosmochimica Acta*, *68*(23), 4905–4914. https://doi.org/10.1016/j.gca.2004.05.033

Szitkar, F., Dyment, J., Choi, Y., & Fouquet, Y. (2014). What causes low magnetization at basalt-hosted hydrothermal sites? Insights from inactive site Krasnov (MAR 16°38′N). *Geochemistry, Geophysics, Geosystems*, *15*(4), 1441–1451. https://doi.org/10.1002/2014GC005284

Szitkar, F., Dyment, J., Fouquet, Y., Honsho, C., & Horen, H. (2014). The magnetic signature of ultramafic-hosted hydrothermal sites. *Geology*, *42*(8), 715–718. https://doi.org/10.1130/G35729.1

Talbot, C. J. (1978). Halokinesis and thermal convection. *Nature*, *273*(5665), 739–741. https://doi.org/10.1038/273739a0

Talwani, M., & Heirtzler, J. R. (1964). *Computation of magnetic anomalies caused by two dimensional structures of arbitrary shape* (Vol. 1, pp. 464–480). Stanford University Publications: Geological sciences. https://doi.org/10.1029/2019GL082767

Tivey, M. A., & Dyment, J. (2010). The magnetic signature of hydrothermal systems in slow spreading environments. In P. A. Rona, C. W. Devey, J. Dyment, & B. J. Murton (Eds.), *Diversity of hydrothermal systems on slow spreading ocean ridges*. https://doi.org/10.1029/2008GM000773

Tivey, M. A., Rona, P. A., & Schouten, H. (1993). Reduced crustal magnetization beneath the active sulfide mound, TAG hydrothermal field, Mid-Atlantic Ridge at 26°N. *Earth and Planetary Science Letters*, *115*(1–4), 101–115. https://doi.org/10.1016/0012-821X(93)90216-V

Tivey, M. K. (2007). Generation of seafloor hydrothermal vent fluids and associated mineral deposits. *Oceanography*, *20*(1), 50–65. https://doi.org/10.5670/oceanog.2007.80

Wessel, P. (2010). Tools for analyzing intersecting tracks: The X2SYS package. *Computers & Geosciences*, *36*(3), 348–354. https://doi.org/10.1016/j.cageo.2009.05.009

Xu, W., Xie, L., Aoki, Y., Rivalta, E., & Jónsson, S. (2020). Volcano-wide deformation after the 2017 Erta Ale dike intrusion, Ethiopia, observed with radar interferometry. *Journal of Geophysical Research: Solid Earth*, *125*(8), e2020JB019562. https://doi.org/10.1029/2020JB019562

Zierenberg, R. A., Adams, M. W. W., & Arp, A. J. (2000). Life in extreme environments: Hydrothermal vents. *Proceedings of the National Academy of Sciences of the United States of America*, *97*(24), 12961–12962. https://doi.org/10.1073/pnas.210395997

Journal of Geophysical Research: Solid Earth

Supporting Information for

Magnetic Signature of Active Hydrothermal Systems in a Volcanic-Evaporitic Environment in the Danakil Depression

Hanjin Choe[1], Jerome Dyment[2], and Daniel Mège[3,4]

[1] Department of Geological Sciences, Pusan National University, Busan, 46241, Republic of Korea

[2] Université Paris Cité, Institut de physique du globe de Paris, CNRS, 1 rue Jussieu, 75005 Paris, France

[3]Centrum Badań Kosmicznych Polskiej Akademii Nauk (CBK PAN), Bartycka 18A, 00-716 Warszawa, Poland

[4]Physikalisches Institut, Universität Bern, Sidlerstr. 5, 3012 Bern, Switzerland

Contents of this file

Additional Supporting Information (Files uploaded separately)

Supporting Data Sets 1 (magnetic anomaly grid profiles and 11 separate profiles) provides the GPS location and magnetic field values of the magnetic grids and profiles collected during the survey. Grids and profile data are collected in the spread sheet file. Each profile and grid is organized on a separate sheet. The dataset download is available at the data repository Zenodo (https://zenodo.org/records/13845616)

Introduction

The study area is limited in collecting various geophysical datasets due to the harsh environment and only a few studies explain geological characteristics in this area although geologically unique place on Earth. Therefore, we analyzed using various methodologies including satellite topography analysis, field photos, and magnetic data analysis. The results supporting the main parts of the paper are described in this document.

Contents

Text S1.

Introduction

In this study, we propose that the source of the observed magnetic anomalies in the northern zone of the Yellow Lake Fissure (YLF) area at Grid 1 is a dark red patch exposed at the surface of the dry lake Karum, extending to a shallow depth (<1 m). This feature, which emerges as a topographic high during periodic flooding events, is referred to as Island Dome. These floods, driven by rainwater runoff from the Afar rift margin mountains, increase the water level of Lake Karum, pushing the shoreline northward toward Dallol. Satellite images (Table S2) capture these dynamic changes, providing insights into the horizontal extent and topographic shape of Island Dome.

The central part of the positive magnetic anomaly in Grid 1 (Figure S2c) aligns with the surface exposure of this red mud patch, while the maximum extent of Island Dome corresponds to the measured extent of the magnetic anomaly. To better understand this feature and its surroundings, we analyzed both satellite imagery and two independent topographic datasets.

Topographic analysis for horizontal extent of Island Dome

The horizontal extent of the Island Dome can be inferred from the satellites. Table S2 provides a list of satellite images that help characterize the Island Dome. It includes images which captured water from Lake Karum propagating toward Dallol in response to runoff from catchments in the Afar margin mountains and the Danakil Alps. Water level variations make it possible to determine shape of the island topography. Table S2 also includes high-resolution satellite images showing the surface exposures of the interpreted magnetic formation.

Topographic Characterization using Drone-Based DTM and GPS Data

The topography of the Island Dome could be characterized using two topographic sources.

1. Drone-based digital terrain model (DTM)

We analyzed a DTM of Grid 1 obtained by stereophotogrammetric processing of drone-captured imagery conducted during the magnetic field campaign, with a pixel size of 1x1 m, kindly provided by Pascal Allemand, Claude Bernard University, Lyon. This topography dataset is vertically calibrated.

2. GPS-base relative elevation

Another source of topography is provided by the vertical component of GPS data collected at each magnetic survey data point. Stand-alone GPS receiver vertical error is controlled by systemic processes, including broadcast clock and ephemeris, ionospheric and tropospheric delays, and GPS receiver hardware and software (e.g., Conley et al., 2005).

The GPS receiver (Garmin 62s) was switched on without interruption during each field campaign day. Stable weather conditions during day time during the magnetic measurement field campaign helped stabilize the relative elevation error while collecting data along a given magnetic line.

Assuming that the relative error varies slowly, GPS elevation at the magnetic measurement sites were compared with elevation variations observed in the digital terrain, in an effort to more accurately characterize the Island Dome topography.

We did not attempt to infer vertical accuracy from GPS measurements since the objective of topographic analysis was characterization of the island topography with respect to surroundings. Practically, absolute vertical error of stand-alone GPS has been reported to be at the scale of several meters, and receiver-dependent, preventing from a general rule or correction scheme to be useful. The collected GPS data we collected also show vertical errors at the scale of meters.

3. Topographic profile measurement

The topography of the Island Dome was investigated along East-West and North-South profiles centered on Grid 1. East-West profiles are constrained by the drone-based DTM as well as GPS data. Topography was analyzed along four Grid 1 magnetic lines: G1L3, G1L4, G1L5, G1L6. Only DTM data constrain topography in the North-South direction, because data spacing in the North-South direction is 100 m (Table S1). Four such profiles were investigated: G1C1, G1C2, G1C3, G1C4.

References

Conley, R., R. Cosentino, C. Hegarty, E. Kaplan, J. Leva, M.U. de Haag, and K. Van Dyke. Performance of Stand-Alone GPS. In: E.D. Kaplan, and C.J. Hegarty, Editors. Understanding GPS: Principles and Applications, chap. 7, 2nd edn., Artech House, 301-378, 2005.

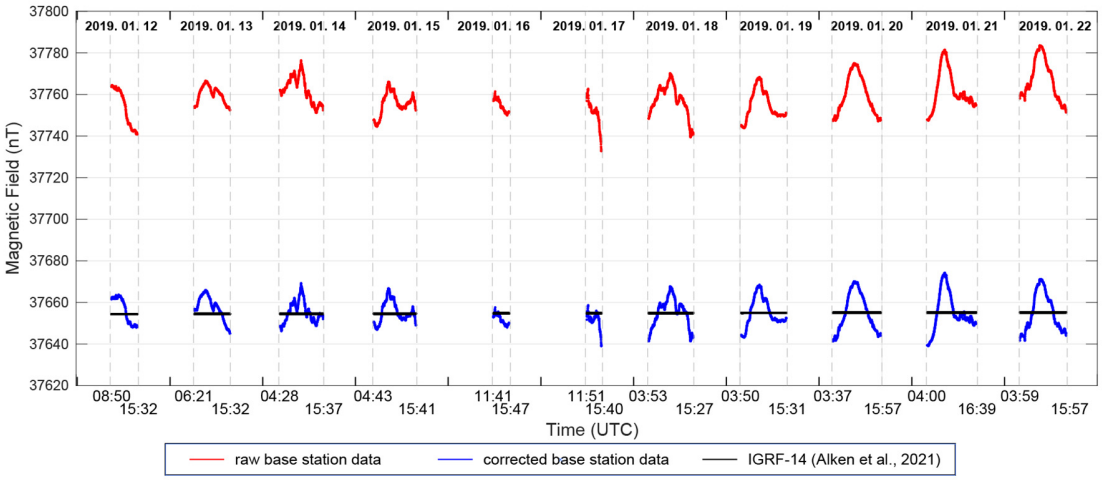

Figure S1. Correction of the base station magnetic data for instrumental drift. The plot compares the raw base station data (red line) with the IGRF-14 model value (black horizontal line) and the final corrected data (blue line). The raw data shows a significant downward drift over the survey period, which is an instrumental error. This drift and a daily offset were removed by aligning the daily mean of the raw data to the corresponding IGRF-14 value. The resulting corrected data reveals the diurnal variation of the Earth's magnetic field, which was subsequently used to correct the mobile survey data. The base station was located at the YARA mining camp (14° 13.99' N, 40° 13.48' E), where electromagnetic interference was minimized.

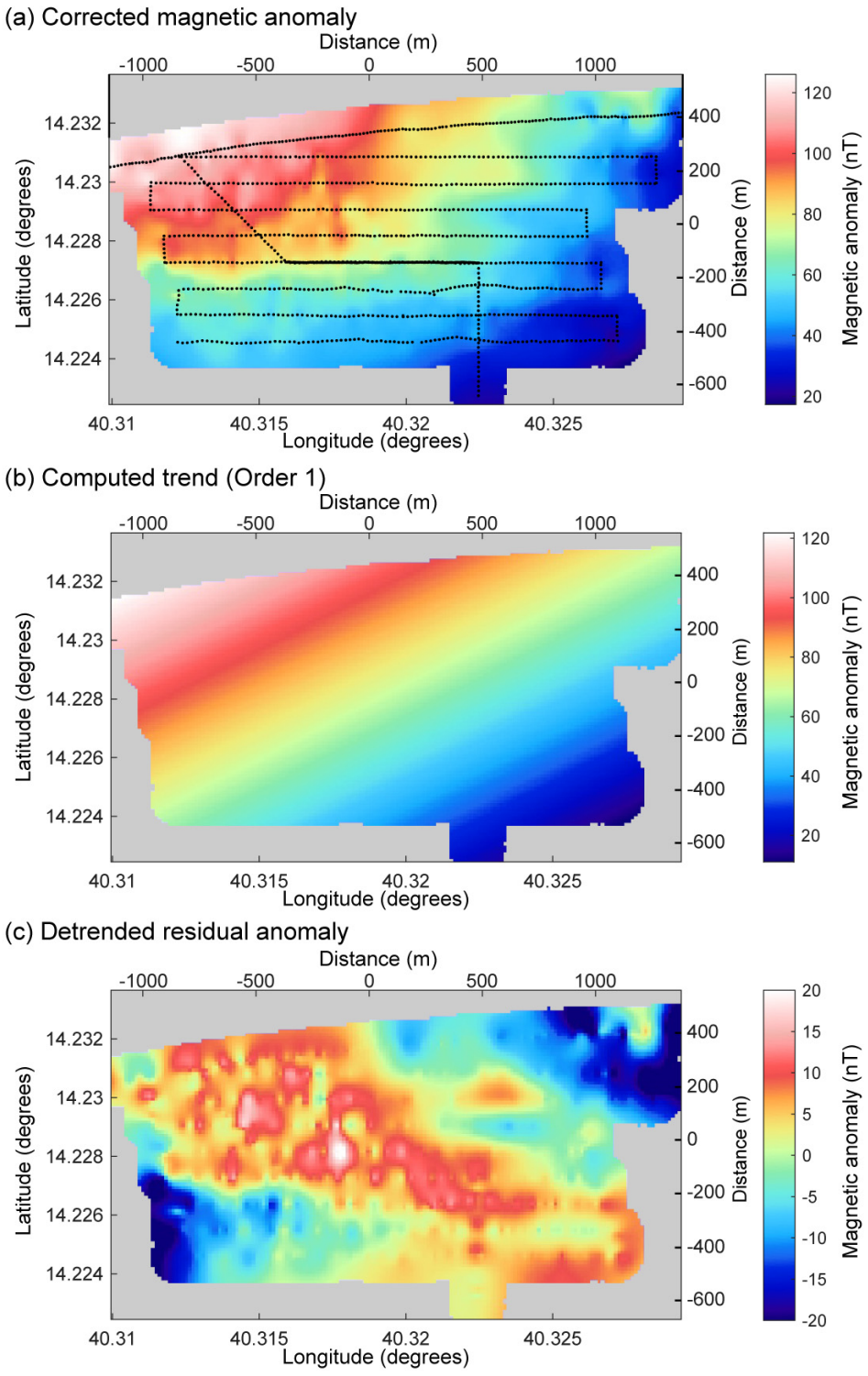

Figure S2. Detrending process of the magnetic anomaly data of Grid 1 to isolate local features. **(a)** The original magnetic anomaly. **(b)** The first-order polynomial plane (linear trend) computed by the least-squares method. **(c)** The residual magnetic anomaly obtained by removing the trend in (b) from the original data.

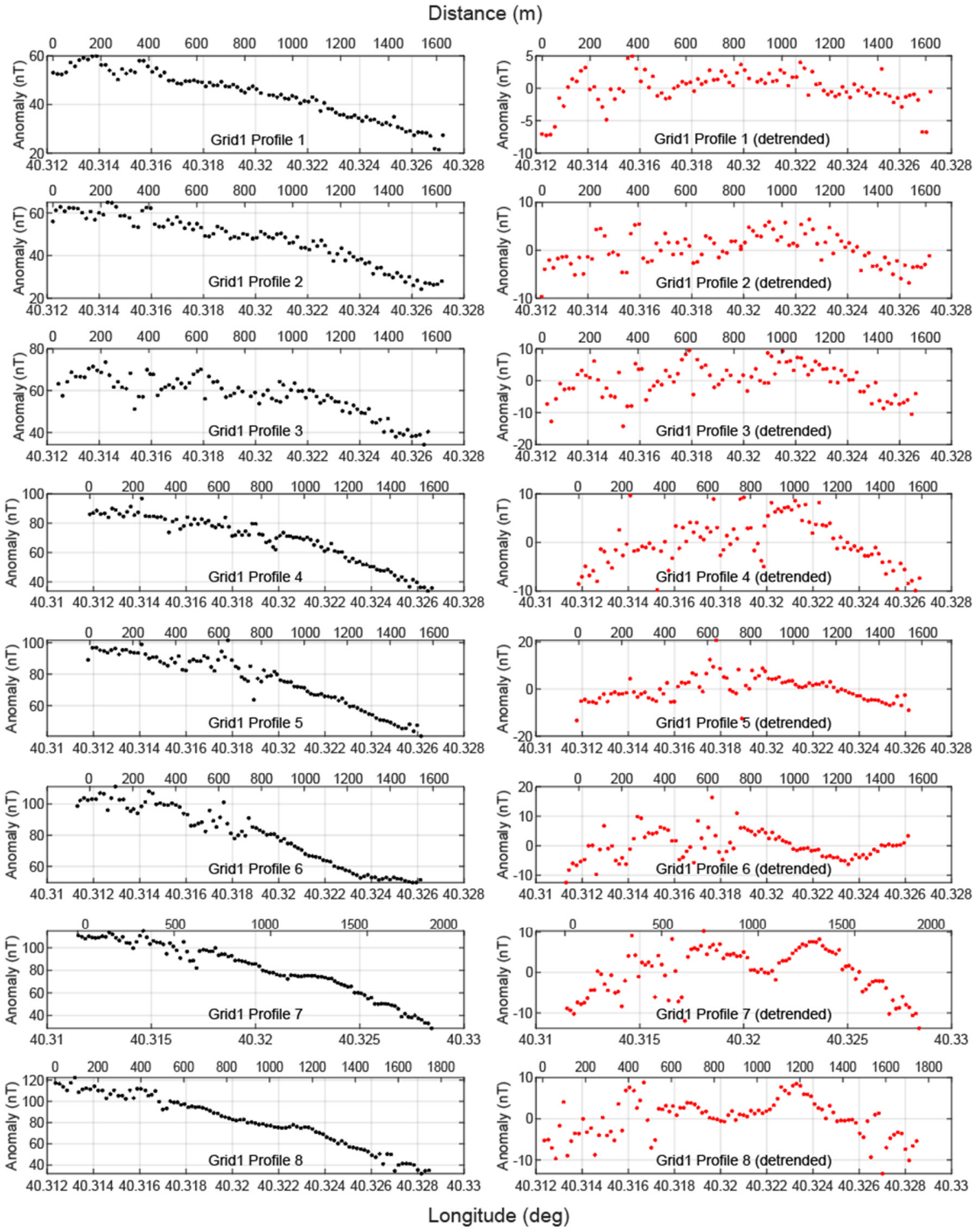

Figure S3. Comparison of original (left column, black dots) and detrended (right column, red dots) magnetic anomaly data for Grid1 E-W profiles 1-8. The x-axes show both longitude (bottom) and distance in meters (top).

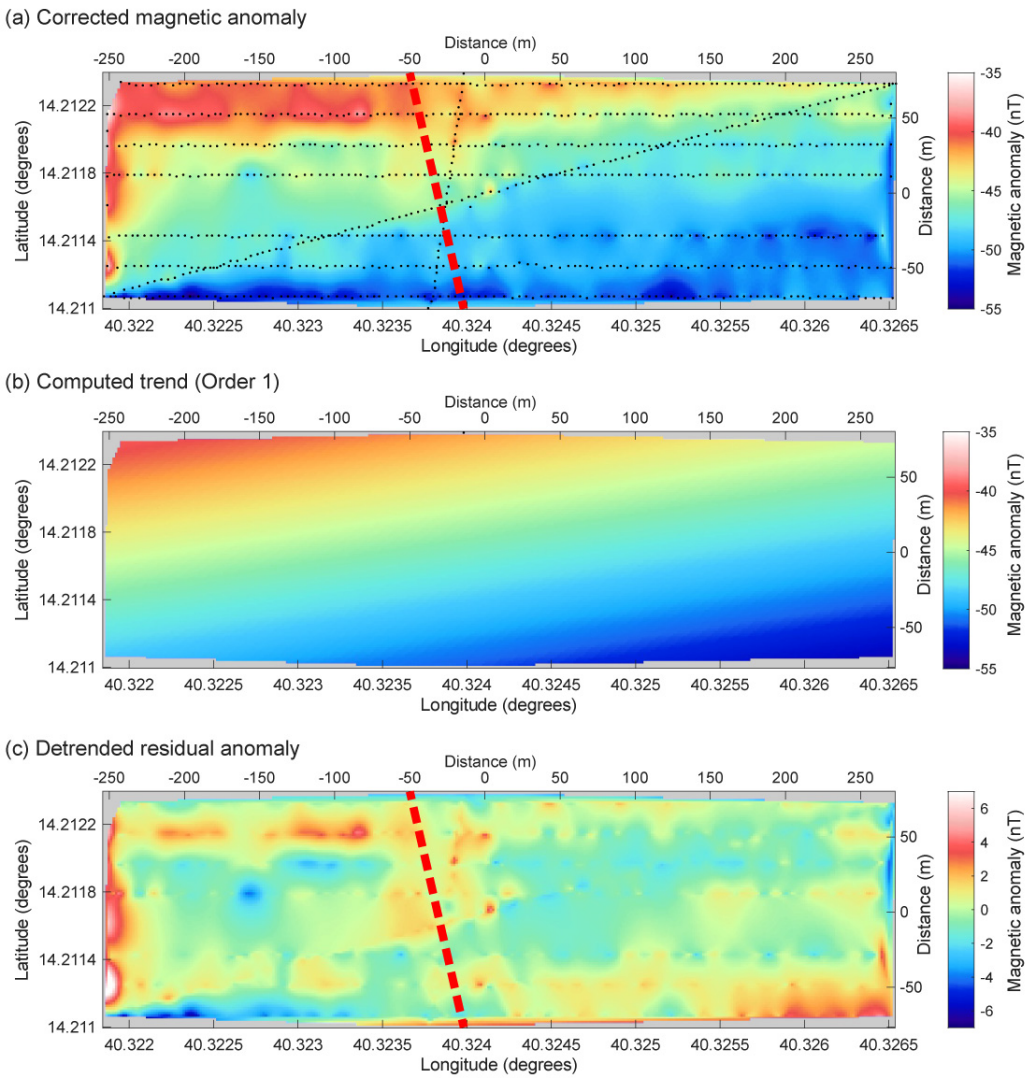

Figure S4. Detrending process of the magnetic anomaly data of Grid 2 to isolate local features. **(a)** The original magnetic anomaly. **(b)** The first-order polynomial plane (linear trend) computed by the least-squares method. **(c)** The residual magnetic anomaly obtained by removing the trend in (b) from the original data. The red dashed lines indicate the YLF across the grid2

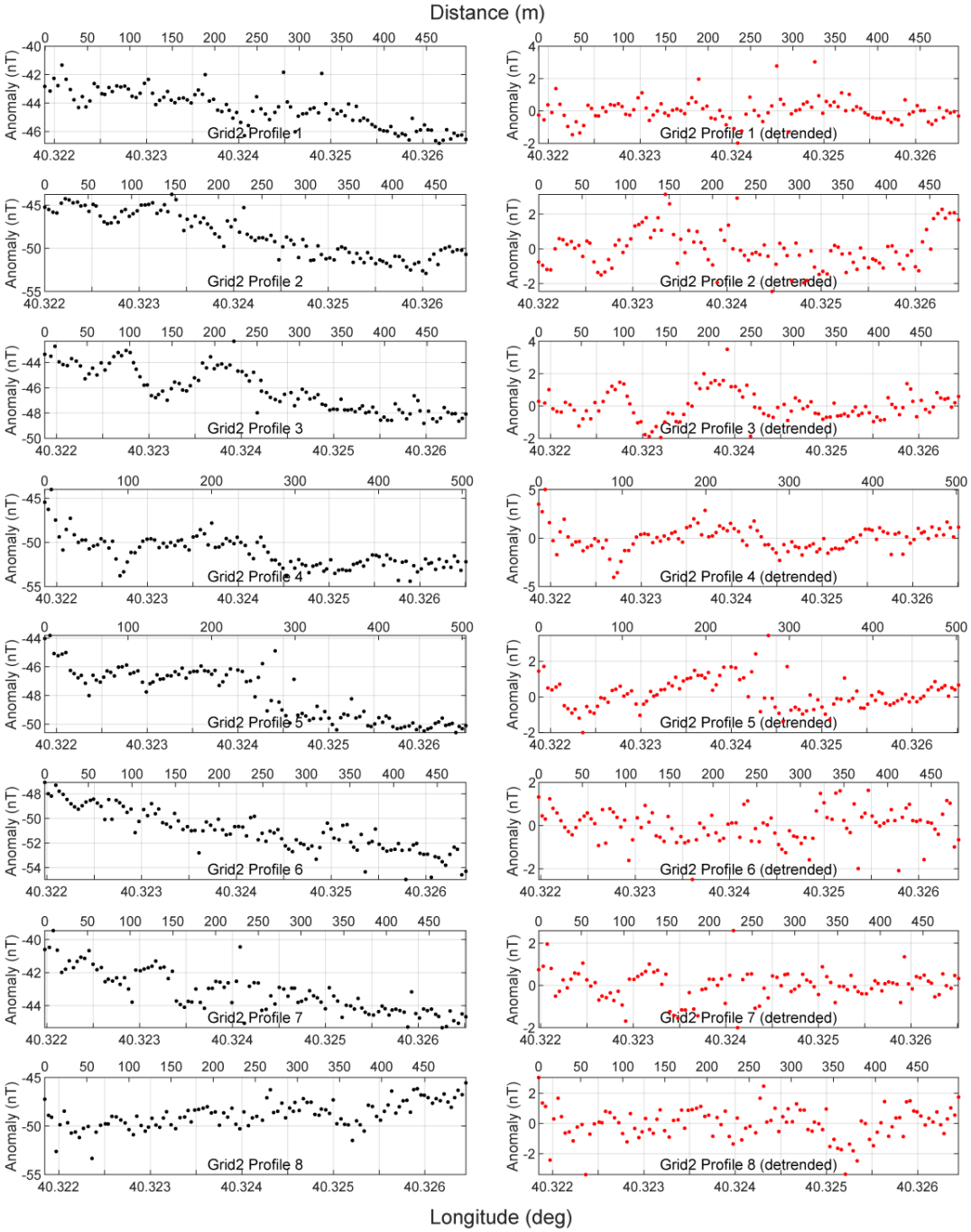

Figure S5. Comparison of original (left column, black dots) and detrended (right column, red dots) magnetic anomaly data for Grid2 E-W profiles 1-8. The x-axes show both longitude (bottom) and distance in meters (top).

150

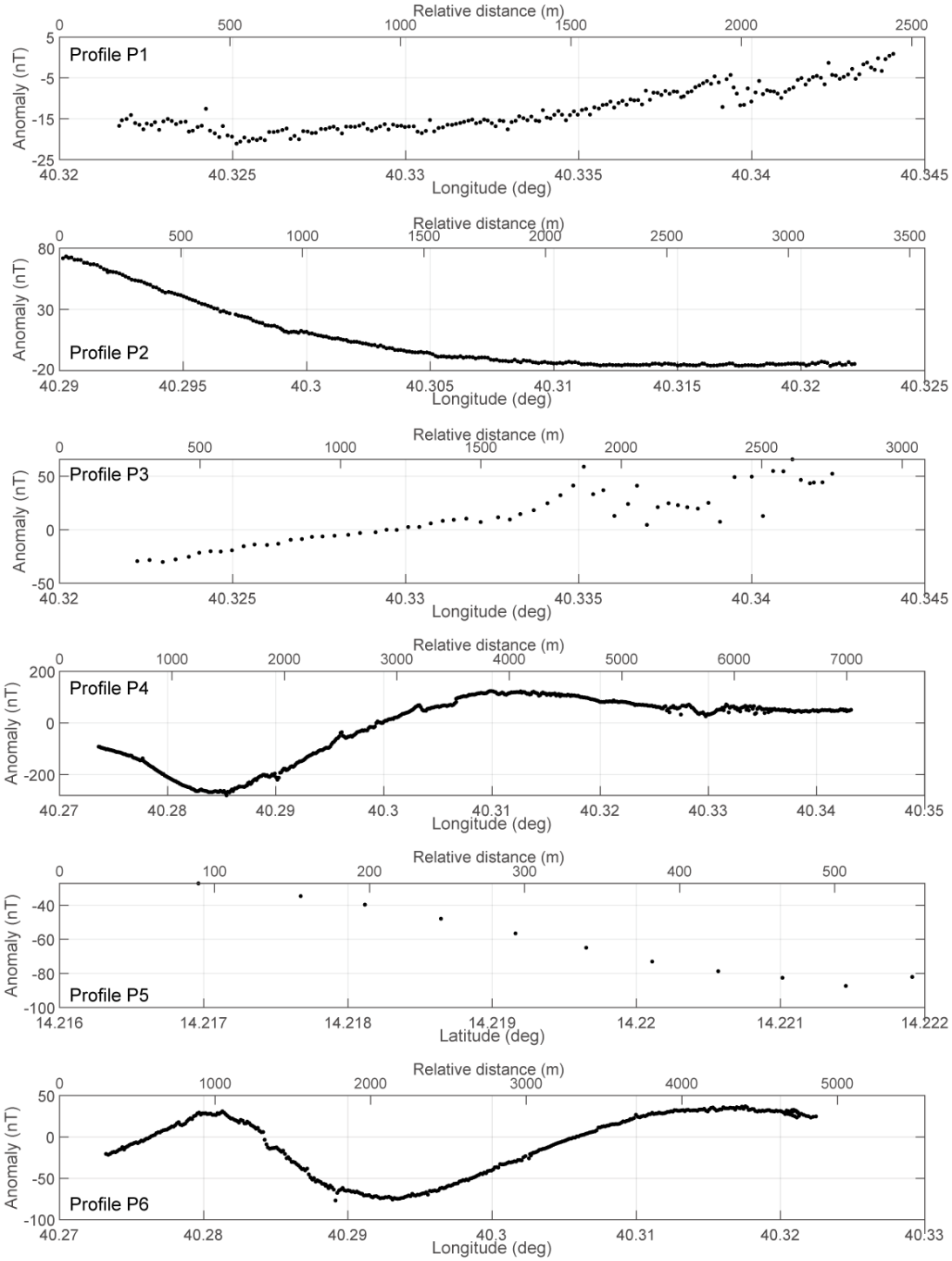

151

152 Figure S6a. Magnetic anomaly profiles from P1 to P6.

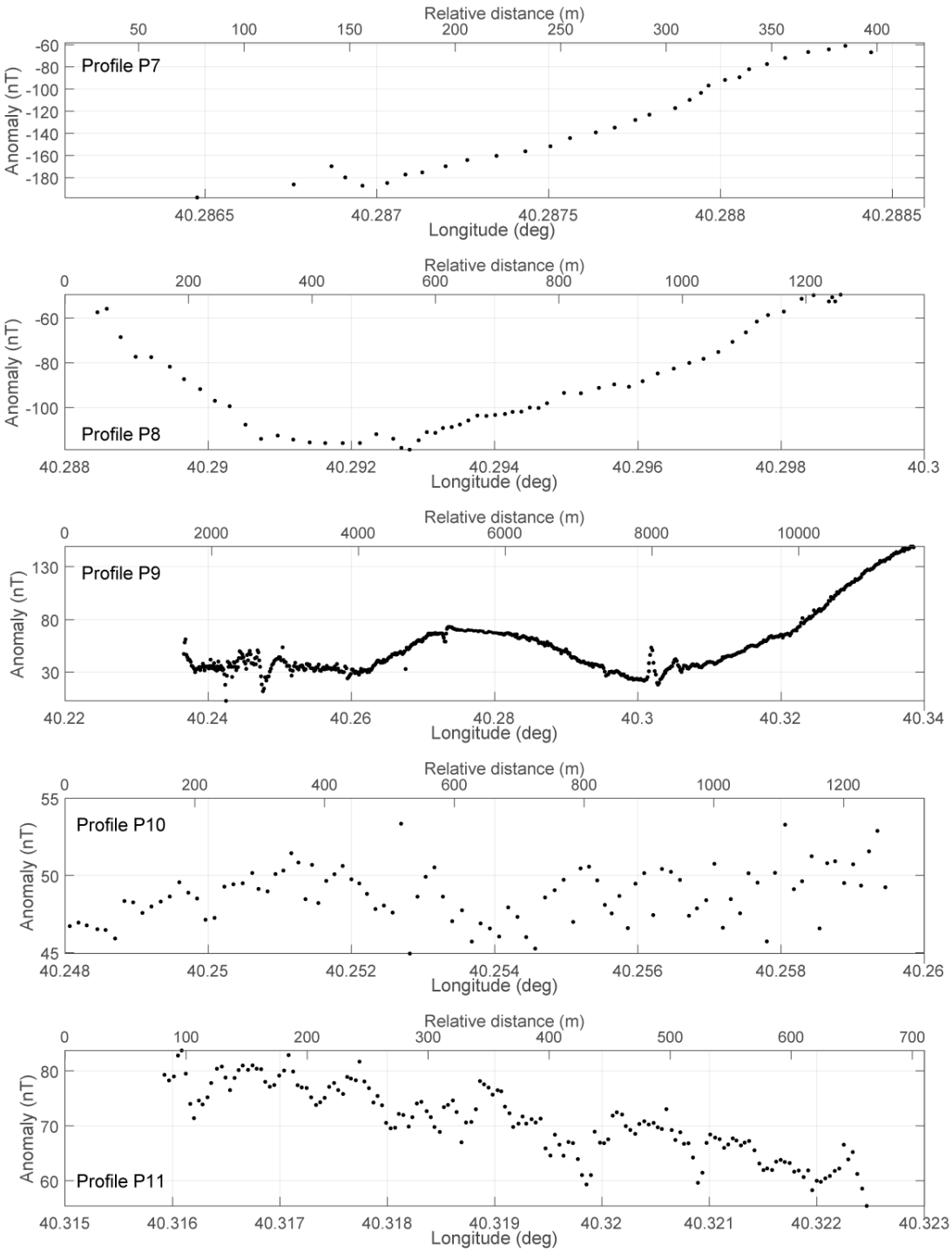

Figure S6b. Magnetic anomaly profiles from P7 to P11.

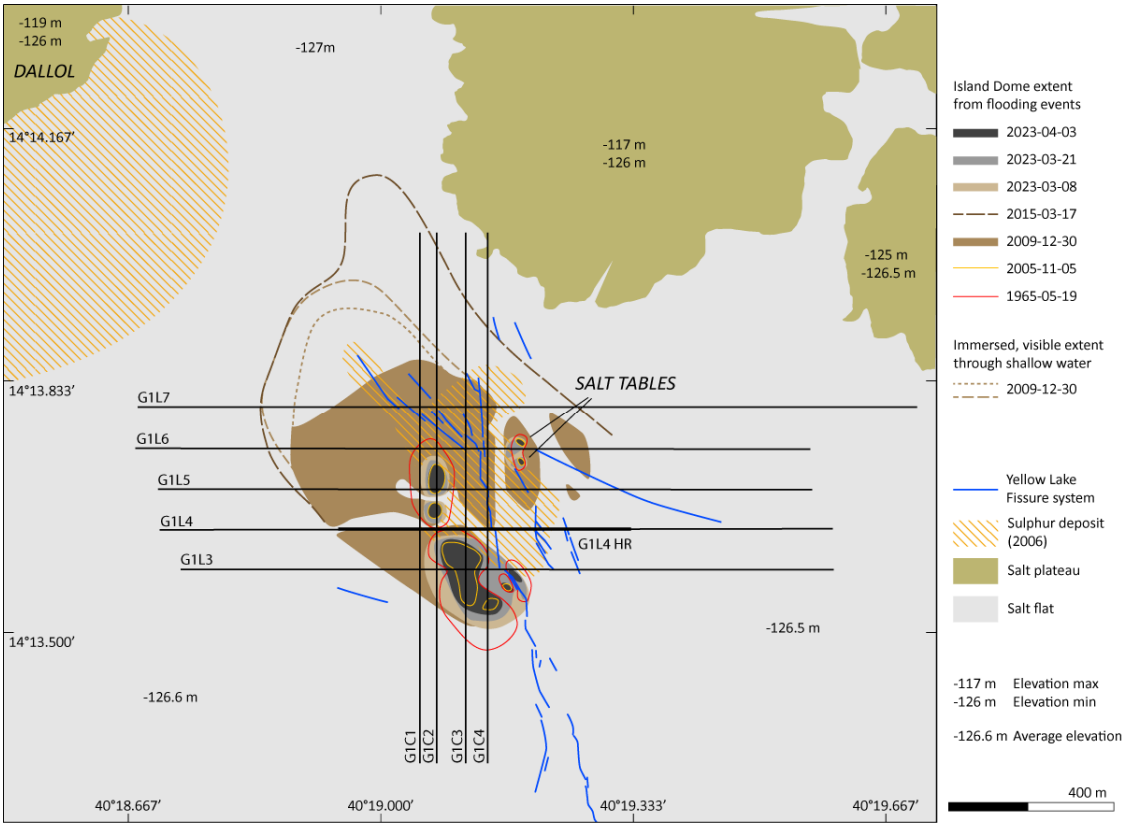

Figure S7. Island Dome shape and location of the studied topographic profiles. Island shape is determined using contours from flood events. From the inner to outermost contours, the flood events have been interpreted from satellite images taken on 19-05-1965, 11-05-2005, 30-12-2009, 17-03-2015, 08-03-2023, 21-03-2023, 03-04-2023 (Table S2).

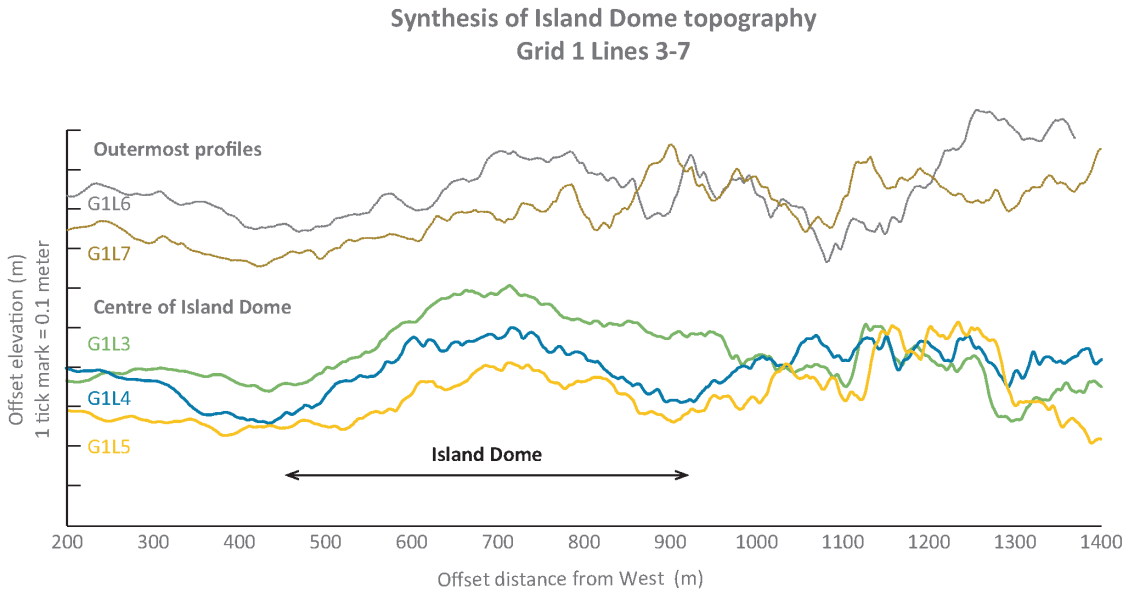

Figure S8. Comparison between East-West topographic profiles highlighting the topography of Island Dome. The profiles were derived from an UAV-based Digital Terrain Model (DTM) survey (methodology described in Mège et al., 2023, section 3.2).

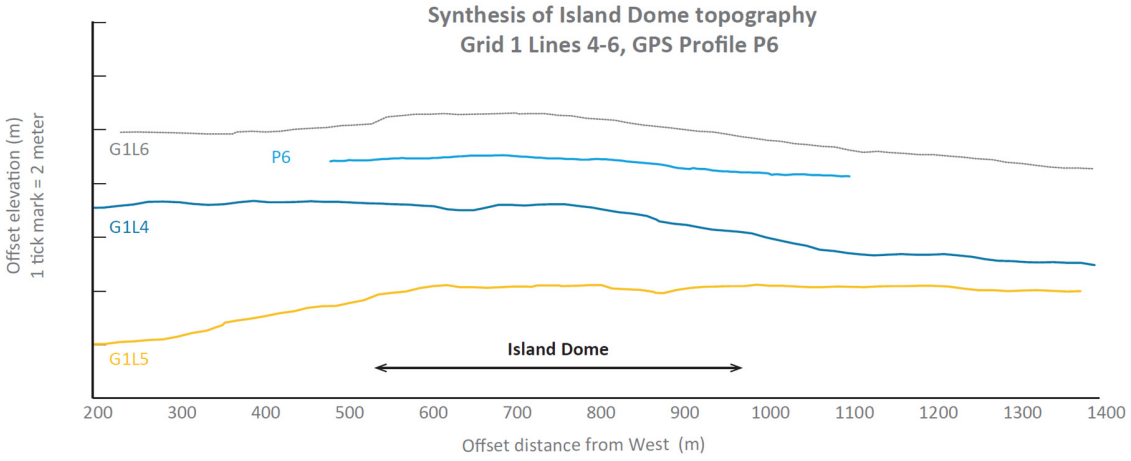

Figure S9. Comparison between East-West topographic profiles from GPS ground observations, highlighting the Island Dome topography. Profile P6 is a high-resolution profile (spacing 4.5 m) located within G1L4. Profiles G1L3 and G1L7 were omitted due to aberrant elevations (G and L stand for Grid and Line, see Figure S7 for locations).

175

ID	Profile	Latitude	Longitude	Alt(m)
YARA MAG Base station	N/A	N14°13.98858'	E040°13.48302'	-122.5
SHORE	N/A	N14°05.96610'	E040°20.31996'	-130.1
P1 MUD LINE	P1	N14°12.88302'	E040°19.84608'	-122.8
P1 MUD	P1	N14°12.91278'	E040°19.95612'	-121.6
NDALLOL POOL1	Near P9	N14°14.5835'	E040°15.9922'	-123.5
NDALLOL POOL2	Near P9	N14°14.5604'	E040°16.0236'	-119.1
NDALLOL POOL3	Near P9	N14°14.5474'	E040°16.0434'	-124.1
NDALLOL POOL4NEW	Near P9	N14°14.5027'	E040°16.0827'	-120.6
NONAME MTN PAN360	Near P9	N14°14.4635'	E040°16.0711'	-116.8
FUTURE PUMPING STAT	N/A	N14°16.9325'	E040°17.6131'	-119.9
ROAD TO EAST	N/A	N14°06.5777'	E040°20.7247'	-120
LIN FRACTURED PLATES	P2	N14°12.7443'	E040°18.9687'	-119.8
RD	P2	N14°12.7190'	E040°18.8530'	-118.9
LIN2	P2	N14°12.7101'	E040°18.7918'	-120.2
RD2	P2	N14°12.6931'	E040°18.6944'	-122
P2 DALLOL ROAD	P2	N14°12.6808'	E040°18.6119'	-121.1
FIS1	P3	N14°12.8477'	E040°19.4123'	-131.5
P3 RED MOUND1	P3	N14°13.3226'	E040°19.8703'	-129
P3 RED MOUND2	P3	N14°13.3146'	E040°19.8526'	-126.1
P3 RED MOUND3	P3	N14°13.5117'	E040°20.1458'	-121.3
P4 SALT MOUND	P4	N14°13.9163'	E040°19.9022'	-116
P4 SALT MOUND2	P4	N14°13.9160'	E040°19.6220'	-120.2
UPLIFT PLATES	P4	N14°13.7213'	E040°18.1013'	-128.7
UPLIFT PL END	P4	N14°13.6943'	E040°18.0050'	-127.8
BUTTES	P4	N14°13.5638'	E040°17.4889'	-126
DALLOL SMALL BULGE	P4	N14°13.5403'	E040°17.3592'	-125.3
SULFUR ZONE	P4	N14°13.5127'	E040°17.2454'	-124.8
SALT NODULES	P4	N14°13.4682'	E040°17.0993'	-123.8
BIS CASCADE BUBBL	P7	N14°13.1970'	E040°17.2609'	-116.3
DYKE 2004	P6	N14°13.1644'	E040°17.6755'	-126.9
ORANGE PATCHES	P9	N14°15.4717'	E040°16.9150'	-119.6
BIG LAKE	P9bis	N14°14.7450'	E040°14.2820'	-122.8
STEPS	P9bis	N14°14.5909'	E040°14.8236'	-121.3

SINKHOLES	P9bis	N14°14.6072'	E040°14.6555'	-123.4
MUD FIELD	P9bis	N14°14.6356'	E040°14.5469'	-119.8
UPLIFTED SALT	P9bis	N14°14.6482'	E040°14.5372'	-120.3
SOFT GROUND	P9bis	N14°14.6483'	E040°14.4447'	-118.5
MICRODIAPIRIC STRUCTURES	P9bis	N14°14.6987'	E040°14.2039'	-120.8
STILL MICRODIAP	P9bis	N14°14.6861'	E040°14.1343'	-119.3
ROUGH PLATES	P9	N14°15.8139'	E040°18.5230'	-123.9
ROUGH PL END	P9	N14°15.8295'	E040°18.6330'	-123.8
ROUGH PL 2	P9	N14°15.9653'	E040°19.1968'	-122.6
ROUGH PL2 END	P9	N14°16.0361'	E040°19.4944'	-123.1
RED PLATES	P9	N14°16.0429'	E040°19.5226'	-123.7
PINK SOIL	P9	N14°16.0466'	E040°19.5413'	-123.4
DEF PL SAMPLE	P9	N14°16.0996'	E040°19.8209'	-121.8
ORANGE PL SULFUR	P9	N14°16.1313'	E040°19.8943'	-121.1
MUD AROUND PL	P9	N14°16.1961'	E040°20.2207'	-117.9
WET MUD	P9	N14°16.1975'	E040°20.2303'	-117.8
END SLIPPERY MUD W SALT	P9	N14°16.1921'	E040°20.2760'	-117.8
WET BEIGE MUD SOFT	P9	N14°16.1904'	E040°20.2861'	-117.2
END PAORAMA	P9	N14°16.1845'	E040°20.2760'	-117.6
SULFUR PINK PLATES3	Near P9	N14°16.3878'	E040°20.1725'	-118.5
DEAD SULFUR POOL NETWORK	Near P9	N14°16.4077'	E040°20.1756'	-118.4
BRINE POOLS	Near P9	N14°16.4426'	E040°20.1724'	-119.5
CRYSTALISING BRINE	Near P9	N14°16.4489'	E040°20.1604'	-119.4
TRANSITIQN OR WHITE BRINE	Near P9	N14°16.4277'	E040°20.1662'	-120.3
MICRODIAP	P9bis	N14°14.7268'	E040°14.1750'	-117.1
UP AND DOWN STR	P9bis	N14°14.6644'	E040°14.0814'	-116.3
MUDDY WET	P9bis	N14°14.6349'	E040°14.0017'	-116.3
GRAVEL SAMPLE	P9bis	N14°14.4205'	E040°13.4494'	-112.6
SAND	P9bis	N14°14.3641'	E040°13.2603'	-109
PEBBLES	P9bis	N14°14.3533'	E040°13.2281'	-108.6
DUNE	P9bis	N14°14.3359'	E040°13.1660'	-105.8
DUNE2	P9bis	N14°14.3304'	E040°13.1384'	-105.4
CLOSED BB POOL1	N/A	14°12.8680'	040°19.2619'	-128.8
CLBBP2	N/A	14°12.8737'	040°19.2578'	-128
CLBBP3	N/A	14°12.8754'	040°19.2529'	-127.6

LIN N060	Grid1	14°13.4752'	040°18.9797'	-117.3
YLFBB1	Grid1	14°13.4536'	040°19.1986'	-117.3
YLFBB2	Grid1	14°13.4662'	040°19.1989'	-117.8
YLFBBP5	Near Grid1	14°13.4157'	040°19.2099'	-115.9
YLFBBP6	Near Grid1	14°13.4090'	040°19.2129'	-115.4
SEGYLF	Near P6	14°13.3907'	040°19.2482'	-115.4
SEGYLF END	Near P6	14°13.3094'	040°19.2650'	-114.8
SEGYLF RELAY	N/A	14°13.3091'	040°19.2675'	-115
SEGYLF2	N/A	14°13.3054'	040°19.2717'	-115.5
SEGYLF2END	N/A	14°13.2966'	040°19.2728'	-115.8
SEGYLF3	N/A	14°13.2922'	040°19.2718'	-115.9
SEGYLF3END	N/A	14°13.2116'	040°19.2955'	-114.5
LINMUD	Near P6	14°13.2044'	040°19.2938'	-116.4
LINMUD END	Near P6	14°13.1445'	040°19.3078'	-117
MUD RIDGE	Near P6	14°13.1436'	040°19.3045'	-117.2
MUD RIDGE END	Near P6	14°13.1002'	040°19.3267'	-117.3
FUMER FIELD	N/A	14°12.9520'	040°19.2629'	-120.3
FUMER FIELD END	N/A	14°12.9878'	040°19.2488'	-120.7
YLF OFF SEGMENT	N/A	14°13.1103'	040°19.2068'	-121.8
NEW WHITE LAKE	Grid1	14°13.5808'	040°19.0723'	-123.8
YLFAA	Grid1	14°13.5769'	040°19.1662'	-124
YLFBB	Grid1	14°13.5669'	040°19.2538'	-125.3
YLFBBP7	N/A	14°12.9752'	040°19.2437'	-126
YLFBBP8	N/A	14°12.9742'	040°19.2497'	-127.1
YLFBBP9	N/A	14°12.9650'	040°19.2488'	-124.2
YLFBBP10	N/A	14°12.9557'	040°19.2532'	-125.1
YLFBBP11	N/A	14°12.9097'	040°19.2635'	-124.5
NNW FIS SEG	Grid1	N14°13.5778'	E040°19.2631'	-131.9
SILENT SEG	Grid1	N14°13.6363'	E040°19.2414'	-126.4
BBSEG	Grid1	N14°13.6348'	E040°19.2026'	-125.3
BB POOL	Grid1	N14°13.6481'	E040°19.2031'	-124.6
BBPOOL2	Grid1	N14°13.6434'	E040°19.2030'	-125.1
YLF SEG PH	Grid1	N14°13.6361'	E040°19.1437'	-124.7
PITTED P	Grid1	N14°13.6428'	E040°19.0781'	-127.6

PH875	Grid1	N14°13.6991'	E040°19.1089'	-120.6
BBPOOL5	Grid1	N14°13.6960'	E040°19.1056'	-121.1
BBPOOL6	Grid1	N14°13.6937'	E040°19.1078'	-120.9
BBPOOL7	Grid1	N14°13.6996'	E040°19.1083'	-122.8
DMSCALE UPLIFT RED	Grid1	N14°13.6927'	E040°19.1279'	-122.5
DMSCALE UPLIFT RED2	Grid1	N14°13.6942'	E040°19.1385'	-121.9
SILENTPOOL2	Grid1	N14°13.7074'	E040°19.1296'	-121.1
BBSEG M UNDERGROUND	Grid1	N14°13.6912'	E040°19.1902'	-121.1
ENTER STICKY AREA	Grid1	N14°13.7439'	E040°19.2964'	-118.4
BB SEG	Grid1	N14°13.7439'	E040°19.1043'	-117.3
BB AREAS	Grid1	N14°13.7444'	E040°19.0952'	-117.2
BB AREAS2	Grid1	N14°13.7433'	E040°19.0480'	-117.4
BBPITTEDPOOL2	Grid1	N14°13.7465'	E040°19.0373'	-118.3
EXIT STICKY AREA	Grid1	N14°13.7437'	E040°18.9433'	-116.8
SULFUR PLATES	Grid1	N14°13.8296'	E040°18.9888'	-118.5
ROAD2YL	P6	N14°13.2715'	E040°18.5970'	-118.6
YLFBBPOOL9	Grid1	N14°13.5470'	E040°19.1878'	-122.1
SULFUR PLATES2	Grid1	N14°13.8505'	E040°18.9829'	-124.2
YLFBBFIS1	Grid2	N14°12.7406'	E040°19.4413'	-126.4
YLBB2	Grid2	N14°12.7398'	E040°19.4933'	-125.8
YLFBBFIS3	Grid2	N14°12.7286'	E040°19.4464'	-125.1

176 **Table S1. The** coordinates of unique geological characteristics in the study area.
177

Date	Satellite platform	Image ID	Resolution (pixel size)*	Note
1965-05-19	Keyhole -4A (CORONA)	DS1021-1009DA051	2.4 m	Earliest evidence of magnetic patch
1984-10-09	Gemini	7S41000601328	18.5 m	Same patch extent as in 1965
2001-10-21	Landsat-7	LE07_L1TP_168050_20011021_20170202_01_T1	15 m (PAN) and 30 (VIS-NIR-SWIR)	Partly flooded island
2003-12-14	Landsat-7	LE07_L1TP_168050_20031214_20170123_01_T1	15 m (PAN) and 30 (VIS-NIR-SWIR)	Partly flooded island
2004-05-06	Landsat-7	LE07_L1TP_168050_20040506_20170121_01_T1	15 m (PAN) and 30 (VIS-NIR-SWIR)	Island almost fully flooded
2005-04-23	ASTER	AST_L1T_00304232005075602_20150509044735_103448	15 m (VIS-NIR) and 30 m (SWIR)	Flooded, only the island peak is emerged
2005-11-05	Spot-5	513832205110507522 92V	10 m (VIS-NIR) and 20 m (SWIR)	Patch distribution after the 2004-2005 hydrothermal crisis
2005-12-17	Orbview-3	3v051217p0001021551a520008501132m_0016256961GST	1 m (PAN)**	Same as 2005-11-05
2008-11-09	Landsat-7	LE07_L1TP_168050_20081109_20161224_01_T1	15 m (PAN) and 30 m (VIS-NIR-SWIR)	Island surrounded by floods
2009-12-06	Landsat-5	LT05_L1TP_168050_20091206_20200825_02_T1	30 m (VIS-NIR-SWIR)	Island surrounded by floods
2015-03-17	Spot-6	2015-03-17 IMG_SPOT6_P_20150317 0724335_ORT_4845944101_R1C1	1.5 m (PAN) and 6 m (VIS-NIR)	Island underlined by paleo-flood albedo patterns
2015-12-23	Landsat-8	LC08_L1TP_168050_20151223_20180526_01_T1	15 m (PAN) and 30 m (VIS-NIR-SWIR)	Island surrounded by floods
2016-05-15	Landsat-8	LC08_L1TP_168050_20160515_20170324_01_T1	15 m (PAN) and 30 m (VIS-NIR-SWIR)	Island surrounded by floods
2018-05-05	Landsat-8	LC08_L1TP_168050_20180505_20180517_01_T1	15 m (PAN) and 30 m (VIS-NIR-SWIR)	Island surrounded by floods
2018-09-10	Landsat-8	LC08_L1TP_168050_20180910_20180913_01_T1	15 m (PAN) and 30 m (VIS-NIR-SWIR)	Island surrounded by floods
2019-10-15	Landsat-8	2019-10-15 LC08_L1TP_168050_20191015_20191029_01_T1	15 m (PAN) and 30 m (VIS-NIR-SWIR)	Island surrounded by floods
2023-03-21	Planetscope	20230321_073304_55_241c_3B_AnalyticMS_SR	3 m (VIS-NIR)	Island flooded to mid elevation
2023-03-31	Planetscope	20230331_065103_56_241d_3B_AnalyticMS_SR	3 m (VIS-NIR)	Lowest part of Island flooded
2023-04-04	Planetscope	20230404_072937_25_2498_3B_AnalyticMS_SR	3 m (VIS-NIR)	Base of Island flooded

2023-04-09	Planetscope	20230409_065117_19_2420_3B_AnalyticMS_SR	3 m (VIS-NIR)	Lowest part of Island flooded
2023-04-17	Planetscope	20230417_064933_26_2442_3B_AnalyticMS_SR	3 m (VIS-NIR)	Base of Island flooded
2023-04-18	Planetscope	20230418_065622_06_24bf_3B_AnalyticMS_SR	3 m (VIS-NIR)	Lower part of Island flooded
2023-04-18	Sentinel-2	S2A_MSIL2A_20230418T073611	10-20 m (VIS-NIR-SWIR)	Lower part of Island flooded

Table S2. Non comprehensive list of satellite images that can help characterize the shape and topography of the Island dome. Some of them have been used to map the island boundaries on Figure S8. PAN = Panchromatic, VIS = visible; NIR = Near-infrared, SWIR = Short-wavelength infrared. *Wavelengths larger than the SWIR range have been discarded. ** Multispectral bands not available.

ID	Acquisition Date (start)	Acquisition Date (end)	startpoint		endpoint		number of points	Data Average Interval (m)	Total Distance (m)
			Lat(deg)	Lon(deg)	Lat(deg)	Lon(deg)			
P1	2019-01-12	2019-01-12	14.213273	40.321724	14.219208	40.344088	194	8.62	1,516.7
P2	2019-01-13	2019-01-13	14.2132	40.322157	14.206593	40.290137	265	15.33	3,662.8
P3	2019-01-14	2019-01-14	14.2329	40.3432	14.2219	40.2736	62	50.4958	3,080.0
P4	2019-01-14	2019-01-15	14.2132	40.3222	14.2325	40.3423	587	13.13	7,690
P5	2019-01-15	2019-01-15	14.2219	40.2736	14.217	40.2732	11	55.813	558.1
P6	2019-01-15	2019-01-22	14.217	40.2732	14.2226	40.3225	429	12.9929	5,560
P7	2019-01-15	2019-01-15	14.2217	40.2865	14.2187	40.2884	32	13.14	407.3
P8	2019-01-15	2019-01-15	14.2187	40.2885	14.2229	40.2988	60	23.589	1,390
P9	2019-01-16	2019-01-18	14.2461	40.2366	14.2698	40.3385	684	17.146	1,170
P9bis	2019-01-17	2019-01-18	14.2433	40.2501	14.244	40.2411	75	13.4209	993.1
P10	2019-01-17	2019-01-17	14.2587	40.2481	14.2625	40.2595	96	13.9412	1,320
P11	2019-01-20	2019-01-20	14.2273	40.3159	14.2273	40.3225	159	4.4934	710.0
Grid1	2019-01-19	2019-01-20	14.2246	40.3122	14.2273	40.3225	1035	16.62	16,200
Grid2	2019-01-21	2019-01-22	14.2123	40.3219	14.211	40.3238	1044	4.93	4,940

Table S3. Summary of track lines for the near-surface magnetic data acquired, detailing coordinates, number of points, and total distance for each line during the campaign.